

# Revealing the Multifunctions of $\text{Li}_3\text{N}$ in the Suspension Electrolyte for Lithium Metal Batteries

Mun Sek Kim, Zewen Zhang, Jingyang Wang, Solomon T. Oyakhire, Sang Cheol Kim, Zhiao Yu, Yuelang Chen, David T. Boyle, Yusheng Ye, Zhuojun Huang, Wenbo Zhang, Rong Xu, Philaphon Sayavong, Stacey F. Bent, Jian Qin, Zhenan Bao, and Yi Cui\*



Cite This: *ACS Nano* 2023, 17, 3168–3180



Read Online

ACCESS |

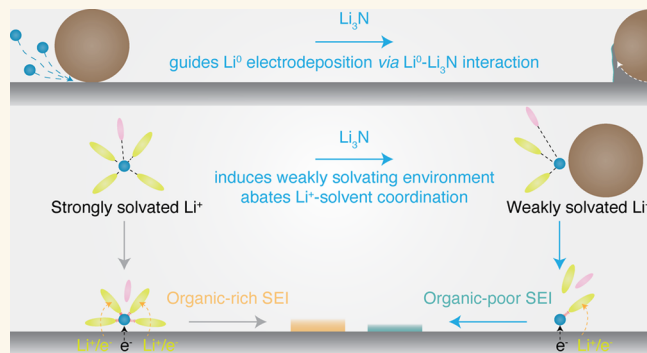
Metrics & More

Article Recommendations

Supporting Information

**ABSTRACT:** Inorganic-rich solid-electrolyte interphases (SEIs) on Li metal anodes improve the electrochemical performance of Li metal batteries (LMBs). Therefore, a fundamental understanding of the roles played by essential inorganic compounds in SEIs is critical to realizing and developing high-performance LMBs. Among the prevalent SEI inorganic compounds observed for Li metal anodes,  $\text{Li}_3\text{N}$  is often found in the SEIs of high-performance LMBs. Herein, we elucidate new features of  $\text{Li}_3\text{N}$  by utilizing a suspension electrolyte design that contributes to the improved electrochemical performance of the Li metal anode. Through empirical and computational studies, we show that  $\text{Li}_3\text{N}$  guides Li electrodeposition along its surface, creates a weakly solvating environment by decreasing  $\text{Li}^+$ -solvent coordination, induces organic-poor SEI on the Li metal anode, and facilitates  $\text{Li}^+$  transport in the electrolyte. Importantly, recognizing specific roles of SEI inorganics for Li metal anodes can serve as one of the rational guidelines to design and optimize SEIs through electrolyte engineering for LMBs.

**KEYWORDS:** lithium–metal battery, lithium metal anode, suspension electrolyte, lithium nitride, solid-electrolyte interphase, lithium solvation environment, electrolyte engineering



## INTRODUCTION

Reversibly utilizing Li metal ( $\text{Li}^0$ ) anodes is a primary step in successfully developing practical high-energy Li metal batteries (LMBs).<sup>1,2</sup> Although the  $\text{Li}^0$  anode involves a classic electroplating/stripping mechanism, achieving highly reversible and electrochemically stable  $\text{Li}^+$  migration at the  $\text{Li}^0$ /electrolyte interface becomes challenging due to the inevitable formation of solid-electrolyte interphases (SEIs) on  $\text{Li}^0$  anodes with electrolytes.<sup>3</sup> Despite the desirable properties of  $\text{Li}^0$  anodes, such as a high theoretical specific capacity of 3,861  $\text{mAh g}^{-1}$  and a low standard electrode potential of  $-3.04$  V versus standard hydrogen electrodes, the high reactivity of  $\text{Li}^0$  makes almost all the possible electrolytes thermodynamically unstable against  $\text{Li}^0$  that decompose electrolyte species to form SEIs, in which the properties of SEIs largely influence the electrochemical performance of  $\text{Li}^0$  anodes.<sup>4–6</sup>

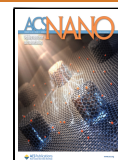
During LMB cycles, solvated  $\text{Li}^+$  must reversibly migrate across the electrolyte and SEIs on  $\text{Li}^0$  anodes, in which characteristics of SEIs predominantly affect  $\text{Li}^+$  transport

behavior.<sup>3</sup> Essentially, SEIs on  $\text{Li}^0$  anodes affect  $\text{Li}^0$  electroplating/stripping and  $\text{Li}^+$  desolvation processes, thereby dictating the electrochemical performance of  $\text{Li}^0$  anodes.<sup>7–9</sup> Despite the critical functions of SEIs on  $\text{Li}^0$  anodes, understanding the roles played by SEI components is still at an early stage to rationally design and manipulate SEIs via electrolyte engineering. As SEI evolutions on  $\text{Li}^0$  anodes are directly linked to the solvation structures of  $\text{Li}^+$  in electrolytes,<sup>3</sup> various modifications to the  $\text{Li}^+$  solvation environment and trends have been investigated to correlate SEI properties that positively impact the electrochemical performance of  $\text{Li}^0$  anodes. In particular, weakly solvating electrolytes and

**Received:** December 16, 2022

**Accepted:** January 23, 2023

**Published:** January 26, 2023



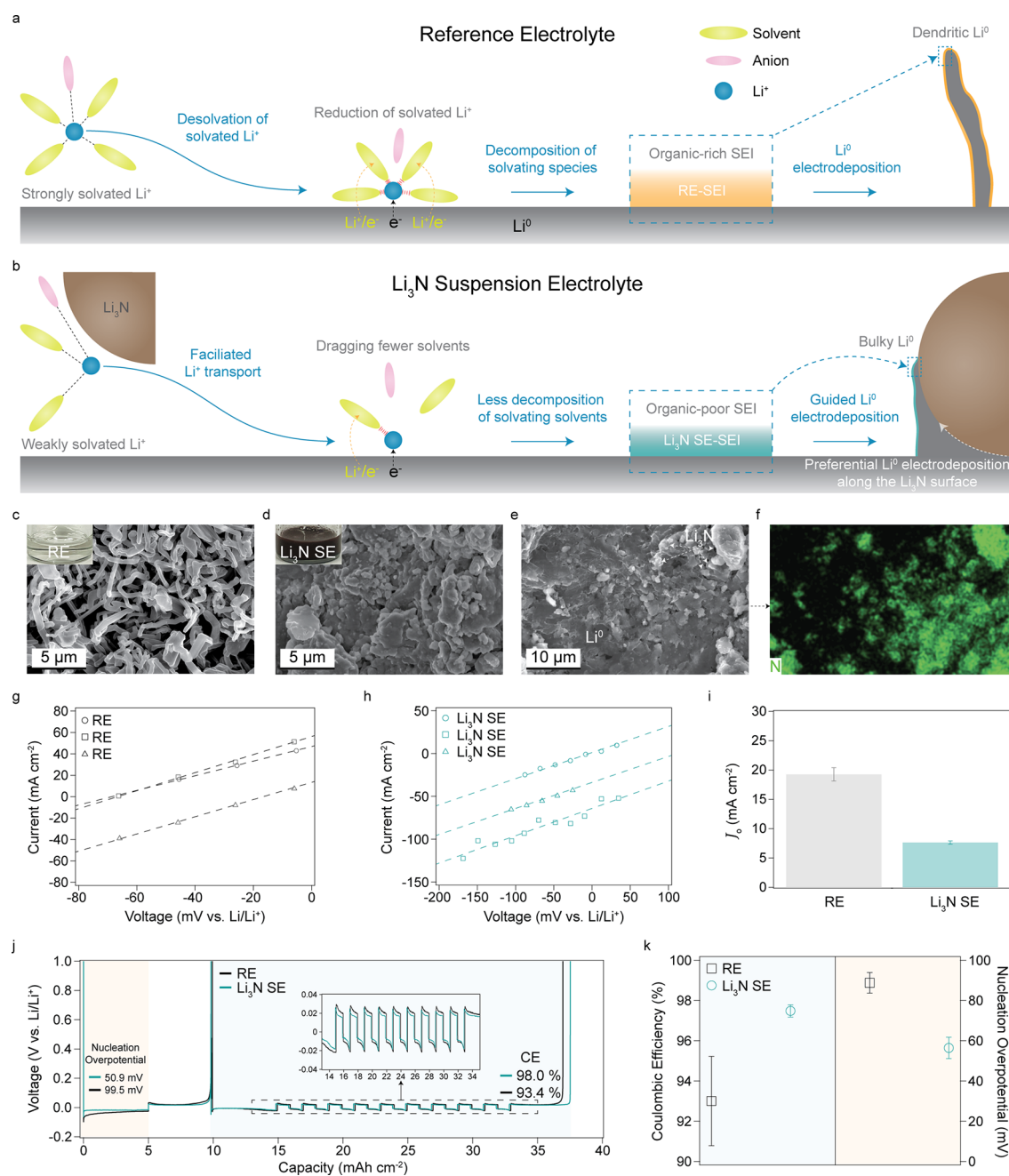


**Figure 1.** Features of  $\text{Li}_3\text{N}$  for  $\text{Li}^0$  anodes. (a) Schematic illustration of strongly solvated  $\text{Li}^+$  in RE impacting the SEI evolution on  $\text{Li}^0$  anodes and  $\text{Li}^0$  electrodeposition. The first step shows  $\text{Li}^+$  desolvation and  $\text{Li}^+$  reduction processes from the solvated  $\text{Li}^+$  in RE. The next step represents the SEI formation on  $\text{Li}^0$  anodes by decomposing solvating species that yield organic-rich SEI. The final step delineates the morphology of dendritic  $\text{Li}^0$  electrodeposits influenced by RE-SEI. (b) Schematic illustration of weakly solvated  $\text{Li}^+$  in  $\text{Li}_3\text{N}$  SE impacting the SEI evolution on  $\text{Li}^0$  anodes and  $\text{Li}^0$  electrodeposition. The first step represents the weakly solvated  $\text{Li}^+$  by  $\text{Li}_3\text{N}$  in the electrolyte, in which fewer solvents are coordinated with  $\text{Li}^+$  relative to that in RE. The next step shows facilitated  $\text{Li}^+$  transport by the decreased  $\text{Li}^+$ -solvent interaction. Then, the weakly solvated  $\text{Li}^+$  suppresses decomposition of solvents by dragging relatively fewer solvent molecules close to the  $\text{Li}^0$  surface that forms organic-poor SEI. The final step shows bulky  $\text{Li}^0$  electrodeposition allowed by the preferential  $\text{Li}^0$  deposition across the  $\text{Li}_3\text{N}$  surface and  $\text{Li}_3\text{N}$  SE-SEI. (c) SEM image of  $\text{Li}^0$  electrodeposits on Cu from Li/Cu cell with RE at  $1 \text{ mA cm}^{-2}$  and  $1 \text{ mAh cm}^{-2}$ . The inset represents the physical image of RE. (d) SEM image of  $\text{Li}^0$  electrodeposits on Cu from Li/Cu cell with  $\text{Li}_3\text{N}$  SE at  $1 \text{ mA cm}^{-2}$  and  $1 \text{ mAh cm}^{-2}$ . The inset represents the physical image of  $\text{Li}_3\text{N}$  SE (e,f), SEM image (e), and corresponding nitrogen elemental mapping (f) of  $\text{Li}^0$  electrodeposits on Cu from Li/Cu cell with exposed  $\text{Li}_3\text{N}$  from  $\text{Li}_3\text{N}$  SE. (g,h) Representative kinetically controlled region from the reverse sweep of ultramicroelectrode cyclic voltammograms for RE (g) and  $\text{Li}_3\text{N}$  SE (h). Three measurements were performed for RE and  $\text{Li}_3\text{N}$  SE. The scan rate and voltage window were  $20 \text{ V s}^{-1}$  and  $-1.75$  to  $2.75 \text{ V vs Li/Li}^+$ . (i) Calculated exchange current density ( $J_0$ ) from g and h for RE ( $19.27 \text{ mA cm}^{-2} \pm 1.13 \text{ mA cm}^{-2}$ ) and  $\text{Li}_3\text{N}$  SE ( $7.64 \text{ mA cm}^{-2} \pm 0.28 \text{ mA cm}^{-2}$ ). (j) Representative voltage profiles of CE measurement from Li/Cu cells with RE and  $\text{Li}_3\text{N}$  SE. The inset represents the zoomed-in voltage profiles from  $13 \text{ mAh cm}^{-2}$  to  $35 \text{ mAh cm}^{-2}$ . The background colors represent where the CE and nucleation overpotential were measured. The applied current density was  $0.5 \text{ mA cm}^{-2}$ . (k) Averaged CE and nucleation overpotential values with standard errors calculated from three identical Li/Cu cells with RE ( $93.01\% \pm 2.21\%$  and  $88.77 \text{ mV} \pm 5.11 \text{ mV}$ ) and  $\text{Li}_3\text{N}$  SE ( $97.48\% \pm 0.31\%$  and  $56.43 \text{ mV} \pm 5.31 \text{ mV}$ ).

inorganic-rich SEIs were found to be beneficial to the electrochemical performance of  $\text{Li}^0$  anodes.<sup>3,6,10–14</sup>

It has been found that SEIs on  $\text{Li}^0$  anodes can swell with electrolytes,<sup>15</sup> indicating that electrolyte species still exist within the SEI domain. This important outcome further justifies the aging of SEIs on  $\text{Li}^0$  anodes.<sup>16</sup> In other words, SEIs are still electrolyte penetrable up to a certain degree, and the electrochemical performance of  $\text{Li}^0$  anodes are, therefore, affected by both SEIs and the electrolyte species. Furthermore, a modified  $\text{Li}^+$  solvation environment by the SEI inorganic compound in the electrolyte has been discovered, which sheds light on the specific features of SEI inorganics that affect SEI evolution and the electrochemical performance of  $\text{Li}^0$  anodes.<sup>6</sup> These combined results suggest that not only can the  $\text{Li}^+$  solvation environment within the SEI region be different from the  $\text{Li}^+$  solvation environment in the electrolyte, but also the electrochemical performance of SEIs on  $\text{Li}^0$  anodes is determined by the distinct SEI inorganic species that sets the specific  $\text{Li}^+$  solvation environment within the SEI layer where the actual  $\text{Li}^+$  desolvation occurs. These insights lead to a critical hypothesis that the  $\text{Li}^+$  solvation shells, not just  $\text{Li}^+$ , can migrate across SEIs, in which the solvated  $\text{Li}^+$  in the bulk electrolyte further gets modified by the specific inorganic species present in the SEIs on  $\text{Li}^0$  anodes. Thus, revealing the roles of inorganic compounds in SEIs is considered one of the fundamental studies to design high-performance SEIs via electrolyte engineering for  $\text{Li}^0$  anodes that will potentially lead to the development of advanced electrolytes for developing reliable LMBs.

Among the frequently observed SEI inorganic compounds (e.g.,  $\text{Li}_2\text{O}$ ,  $\text{Li}_2\text{CO}_3$ ,  $\text{LiF}$ ,  $\text{Li}_3\text{N}$ ,  $\text{Li}_2\text{S}$ , ...),  $\text{Li}_3\text{N}$  was particularly found in almost all the high-performance SEIs of  $\text{Li}^0$  anodes.<sup>3</sup> The beneficial features of  $\text{Li}_3\text{N}$  for  $\text{Li}^0$  anodes from prior studies include thermodynamic stability,<sup>17,18</sup> high  $\text{Li}^+$  conductivity,<sup>19</sup> and  $\text{Li}^0$  dendrite suppression.<sup>20–23</sup> Although various forms of  $\text{Li}_3\text{N}$  (pinhole-free film,<sup>23</sup> nanoflowers,<sup>24</sup> and nanosheets<sup>25</sup>) and electrolyte additives ( $\text{LiN}_3$ <sup>20</sup> and  $\text{LiNO}_3$ <sup>26</sup> to derive  $\text{Li}_3\text{N}$ ) have been applied to improve the electrochemical performance of  $\text{Li}^0$  anodes, there is still an inadequate understanding of the functional mechanism of  $\text{Li}_3\text{N}$  for  $\text{Li}^0$  anodes. Hence, we aim to investigate the further roles of  $\text{Li}_3\text{N}$  in terms of the  $\text{Li}^+$  solvation environment and SEI evolution on  $\text{Li}^0$  anodes that rationalize the working mechanism of  $\text{Li}_3\text{N}$  for  $\text{Li}^0$  anodes and SEIs.

Herein, we designed a  $\text{Li}_3\text{N}$  suspension electrolyte ( $\text{Li}_3\text{N}$  SE) by mixing 80–100 nm  $\text{Li}_3\text{N}$  nanoparticles with a reference electrolyte (RE) of 1 M  $\text{LiPF}_6$  in ethylene carbonate (EC) and diethyl carbonate (DEC) (1:1 v/v) with 10 vol % fluoroethylene carbonate (FEC), in which RE serves as one of the most widely studied electrolytes for the SEI analyses of  $\text{Li}^0$  anodes.<sup>6,8,9,15</sup> Also, the electrolyte blend of RE does not contain any nitrogen species that could form  $\text{Li}_3\text{N}$  through the reduction and/or decomposition of RE species, which will help to closely examine the effect of  $\text{Li}_3\text{N}$  in RE. Moreover, utilizing the suspension electrolyte design allows for revealing the functional mechanism of a particular SEI inorganic compound for LMBs.<sup>6</sup> Thus,  $\text{Li}_3\text{N}$  SE was investigated in detail to identify the  $\text{Li}^+$  solvation environment change, SEI evolution on  $\text{Li}^0$  anodes, and electrochemical performance. By combining the experimental assessments in tandem with first-principles results, we were able to identify new features of  $\text{Li}_3\text{N}$  in the liquid electrolyte for  $\text{Li}^0$  anodes: (i) the surface of  $\text{Li}_3\text{N}$ , especially (001) and (002), is lithiophilic, which guides  $\text{Li}^0$

electrodeposition through a favored  $\text{Li}^0$ - $\text{Li}_3\text{N}$  interaction, (ii)  $\text{Li}_3\text{N}$  creates a weakly solvating environment by decreasing  $\text{Li}^+$ -solvent interaction in the electrolyte, (iii)  $\text{Li}_3\text{N}$  suppresses solvent decomposition to form organic-poor SEI on  $\text{Li}^0$  anodes, and (iv)  $\text{Li}_3\text{N}$  facilitates  $\text{Li}^+$  transport in the electrolyte and  $\text{Li}^0$  interphase. These findings support the progress of comprehending the improved  $\text{Li}^0$  anode performance in connection with the previously reported  $\text{Li}_3\text{N}$  studies and the inorganic-rich SEI concept, particularly having high  $\text{Li}_3\text{N}$  content in the SEIs, of  $\text{Li}^0$  anodes. Significantly, beneficial SEI inorganic compounds induce a weakly solvating  $\text{Li}^+$  environment by modifying  $\text{Li}^+$ -solvent and/or  $\text{Li}^+$ -anion coordination,<sup>6</sup> in which  $\text{Li}_3\text{N}$  is responsible for adjusting  $\text{Li}^+$ -solvent coordination, which affects the electrochemical performance of and SEI evolution on  $\text{Li}^0$  anodes. Consequently, understanding the unique features of SEI inorganic species can potentially provide scientific and rational guidelines to control and design SEIs on  $\text{Li}^0$  anodes by optimizing electrolyte chemistries to improve the electrochemical performance of LMBs.

## RESULTS AND DISCUSSION

**Analyses of  $\text{Li}_3\text{N}$  in the Electrolyte.** Deriving inorganic-rich SEIs by engineering electrolytes became one of the practical approaches to significantly improve the electrochemical performance of  $\text{Li}^0$  anodes for LMBs.<sup>12,13,27,28</sup> Since the SEI evolution on  $\text{Li}^0$  anodes is directly associated with the electrolyte,<sup>3,12,13,28–30</sup> especially its  $\text{Li}^+$  solvation environment, understanding the roles played by the major SEI inorganic components, such as  $\text{Li}_2\text{O}$ ,  $\text{Li}_2\text{CO}_3$ ,  $\text{LiF}$ ,  $\text{Li}_3\text{N}$ , and  $\text{Li}_2\text{S}$ ,<sup>3</sup> can serve as a bridge to connect the mechanism of SEI species and electrochemical performance of  $\text{Li}^0$  anodes.<sup>6</sup> Furthermore, the swelling of SEIs on  $\text{Li}^0$  anodes has recently been identified.<sup>15</sup> It has been shown that the degree of SEI swelling correlates to the electrochemical performance of  $\text{Li}^0$  anodes, in which inorganic-rich or organic-poor SEIs promote superior electrochemical performance of  $\text{Li}^0$  anodes and less SEI swelling.<sup>15</sup> This discovery also leads to an important hypothesis that electrolytes are still present within the SEI layer, where the inorganic compounds in SEIs play an important role in adjusting the  $\text{Li}^+$  solvation environment at the interphase of and SEI evolution on  $\text{Li}^0$  anodes.<sup>6</sup> Since  $\text{Li}_3\text{N}$  is a prominent inorganic that exists in the SEIs of many high-performance  $\text{Li}^0$  anodes,<sup>3,20,26,31–39</sup> this study aims to unveil the important roles of  $\text{Li}_3\text{N}$  in terms of  $\text{Li}^+$  solvation effects as well as  $\text{Li}^0$  electrodeposition stability (Figure 1a,b).

Hypotheses of  $\text{Li}^+$  solvation environment, SEI evolution, and  $\text{Li}^0$  electrodeposition behavior with RE (Figure 1a) and  $\text{Li}_3\text{N}$  SE (Figure 1b) are illustrated to delineate the features of  $\text{Li}_3\text{N}$ . In Figure 1a, the first step represents the desolvation process of strongly solvated  $\text{Li}^+$  by solvents. Then, the solvated  $\text{Li}^+$  in RE gets reduced at the surface of  $\text{Li}^0$  anodes to form organic-rich SEI. Eventually, the SEI derived from RE (RE-SEI) induces dendritic  $\text{Li}^0$  electrodeposition morphology. With  $\text{Li}_3\text{N}$ , the solvated  $\text{Li}^+$  becomes weakly solvated relative to that of RE due to the decrease in the  $\text{Li}^+$ -solvent interaction by  $\text{Li}_3\text{N}$  in the electrolyte (Figure 1b). Please note that the  $\text{Li}^+$ -anion coordination was not affected by the  $\text{Li}_3\text{N}$  in the electrolyte. The weakly solvated  $\text{Li}^+$  in  $\text{Li}_3\text{N}$  SE facilitates the transport of solvated  $\text{Li}^+$  through the electrolyte and  $\text{Li}^0$  interphase. This modified environment of solvated  $\text{Li}^+$  in  $\text{Li}_3\text{N}$  SE then suppresses solvent decomposition to form relatively organic-poor SEI on  $\text{Li}^0$  anodes. Furthermore, the lithiophilic surface of

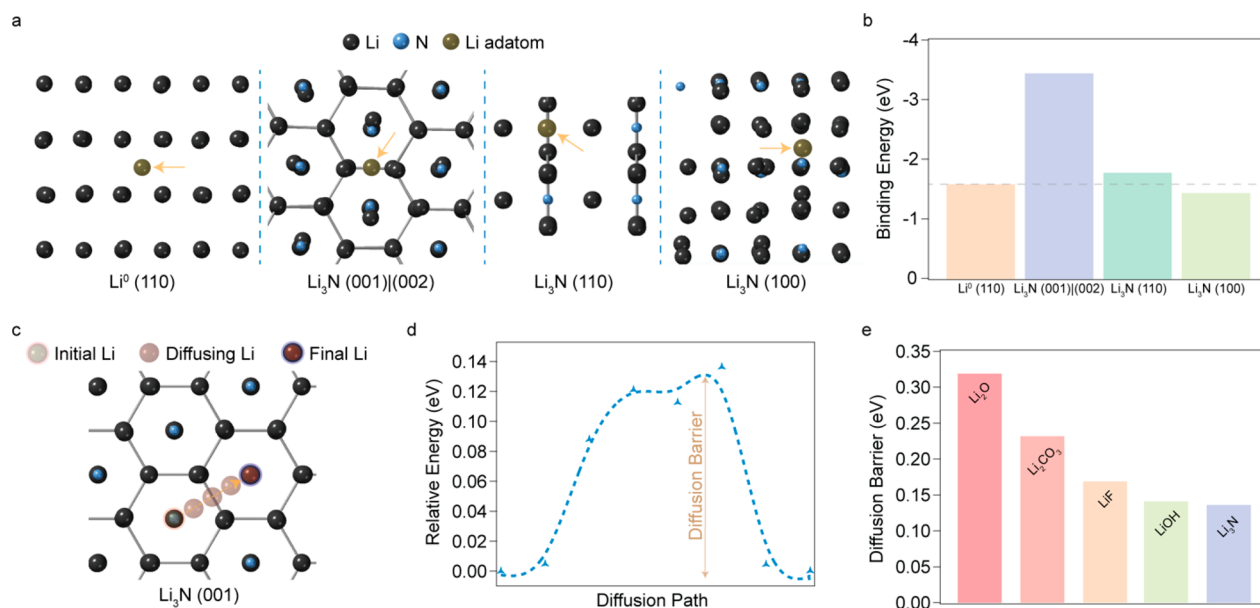


**Figure 2.** DFT analyses of Li<sub>3</sub>N. (a) Li adatom binding sites of Li<sup>0</sup> (110) and Li<sub>3</sub>N (001)|(002), (110), (100) surfaces. The arrows indicate surface adsorbed Li adatom onto the corresponding surfaces of Li<sup>0</sup> and Li<sub>3</sub>N. The color codes for Li of Li<sub>3</sub>N, N, and Li adatom are black, sky-blue, and gray, respectively. (b) Calculated Li adatom binding energies for Li<sup>0</sup> (110), Li<sub>3</sub>N (001)|(002), Li<sub>3</sub>N (110), and Li<sub>3</sub>N (100) surfaces. The dashed gray line indicates the binding energy of Li<sup>0</sup> (110). (c) The Li adatom diffusion pathway across Li<sub>3</sub>N (001) surface. (d) Relative energies based on the Li adatom diffusion trajectories across Li<sub>3</sub>N (001) surface. The diffusion barrier is represented by the magnitude between the highest and lowest relative energies. (e) Li adatom surface diffusion barriers for Li<sub>2</sub>O (0.319 eV), Li<sub>2</sub>CO<sub>3</sub> (0.232 eV), LiF (0.169 eV), LiOH (0.141 eV), and Li<sub>3</sub>N (0.133 eV). The diffusion barriers of Li<sub>2</sub>O, Li<sub>2</sub>CO<sub>3</sub>, LiF, and LiOH were retrieved from the literature.<sup>44</sup>

Li<sub>3</sub>N and the organic-poor SEI derived from Li<sub>3</sub>N SEI (Li<sub>3</sub>N SE-SEI) allow bulky Li<sup>0</sup> electrodeposition. The rest of the discussions are devoted to corroborating these features of Li<sub>3</sub>N for Li<sup>0</sup> anodes.

Observing Li<sup>0</sup> electrodeposition morphologies became a convenient way to anticipate electrochemical characteristics, such as Coulombic efficiency (CE) and Li nucleation overpotential, of Li<sup>0</sup> anodes.<sup>1,40,41</sup> Scanning electron microscopy (SEM) images were examined first to analyze morphological features of Li<sup>0</sup> electrodeposits with RE and Li<sub>3</sub>N SE (Figure 1c–f). High surface area and dendritic Li<sup>0</sup> morphologies were observed with RE (Figure 1c). On the other hand, the Li<sup>0</sup> electrodeposits with Li<sub>3</sub>N SE exhibited nondendritic morphology (Figure 1d). Notably, Li<sub>3</sub>N in Li<sub>3</sub>N SE were embedded into the Li<sup>0</sup> electrodeposits, alluding to preferential Li<sup>0</sup> electrodeposition along the surfaces of Li<sub>3</sub>N (Figure 1d,e). The elemental mapping of nitrogen shown in Figure 1e via energy-dispersive X-ray spectroscopy (EDXS) confirmed that the observed particles were Li<sub>3</sub>N as Li<sub>3</sub>N was the only nitrogen-containing species in Li<sub>3</sub>N SE (Figure 1f). To justify the guided Li<sup>0</sup> electrodeposition toward Li<sub>3</sub>N, the low-magnification SEM image of the electrodeposited Li<sup>0</sup> with Li<sub>3</sub>N SE is shown in Figure S1a. Figure S1a vividly depicts rough surface features due to the Li<sub>3</sub>N network formed by the Li<sub>3</sub>N SE, in which the nitrogen mapping indicates that the topmost part is Li<sub>3</sub>N (Figure S1b). The carbon and oxygen mapping in Figure S1c,d indirectly illustrate Li<sup>0</sup> electrodeposits, as they are the major elements for SEIs on Li<sup>0</sup>. Based on Figure S1a–d, the region that exhibits the height variation due to Li<sub>3</sub>N was selected and shown in Figure S1e, in which the rough surface region was purposefully chosen to demonstrate the preferred Li<sup>0</sup> electrodeposition toward Li<sub>3</sub>N. Figure S1e evidently shows that Li<sup>0</sup> was electrodepositing along the surfaces of Li<sub>3</sub>N as the bottommost surface was free

of Li dendrites, and the Li<sub>3</sub>N was well covered by Li<sup>0</sup> electrodeposits. Hence, the SEM/EDXS analysis suggest that Li<sup>0</sup> tends to get electrodeposited along the surfaces of Li<sub>3</sub>N.

To electrochemically probe possible Li<sup>0</sup>-Li<sub>3</sub>N interactions in Li<sub>3</sub>N SE, the exchange current densities (*J*<sub>0</sub>) for RE and Li<sub>3</sub>N SE were measured with the ultramicroelectrode under a fast scan (20 V s<sup>-1</sup>) cyclic voltammetry (CV) (Figure 1g–i). The fast scan CV with ultramicroelectrode allows for closely investigating electron transfer kinetics of Li with respect to a particular electrolyte by minimizing the effect of mass transports across electrolytes and SEIs on Li<sup>0</sup> electrode.<sup>42</sup> Since *J*<sub>0</sub> reflects the intrinsic rate of electron transfer at the Li<sup>0</sup>/electrolyte interface, any changes in *J*<sub>0</sub> for Li<sub>3</sub>N SE would clearly indicate the existence of Li<sup>0</sup>-Li<sub>3</sub>N interaction, mainly due to the identical liquid electrolyte used for RE and Li<sub>3</sub>N SE. By analyzing the kinetically controlled region<sup>42</sup> in the voltammograms of RE (Figure 1g) and Li<sub>3</sub>N SE (Figure 1h), the averaged *J*<sub>0</sub> for RE and Li<sub>3</sub>N SE were calculated as 19.27 mA cm<sup>-2</sup> ± 1.13 mA cm<sup>-2</sup> and 7.64 mA cm<sup>-2</sup> ± 0.28 mA cm<sup>-2</sup>, respectively (Figure 1i). The noticeable changes in *J*<sub>0</sub> for Li<sub>3</sub>N SE compared to that of RE confirmed the Li<sup>0</sup>-Li<sub>3</sub>N interaction, in which the electron transfer was also occurring at the Li<sup>0</sup>/Li<sub>3</sub>N interface for Li<sub>3</sub>N SE. Also, the Li<sup>0</sup>-Li<sub>3</sub>N interaction probed by the *J*<sub>0</sub> supports the lithiophilic feature of Li<sub>3</sub>N, which is discussed further in the later section. Moreover, the lower value of *J*<sub>0</sub> for Li<sub>3</sub>N SE signifies that the rate of electron transfer with Li<sub>3</sub>N SE was slower compared to that with RE. This is obvious due to the additional electron transfer happening at the Li<sup>0</sup>/Li<sub>3</sub>N interface that should intrinsically be slower than that at the Li<sup>0</sup>/electrolyte interface. Since Li<sub>3</sub>N is a good Li<sup>+</sup> conductor,<sup>19</sup> the charge transfer occurring at the Li<sup>0</sup>/Li<sub>3</sub>N interface further suggests that Li<sup>0</sup> can be electrodeposited and grow from the surfaces of Li<sub>3</sub>N once Li<sub>3</sub>N is in contact with Li<sup>0</sup>. In other words, the heterojunction

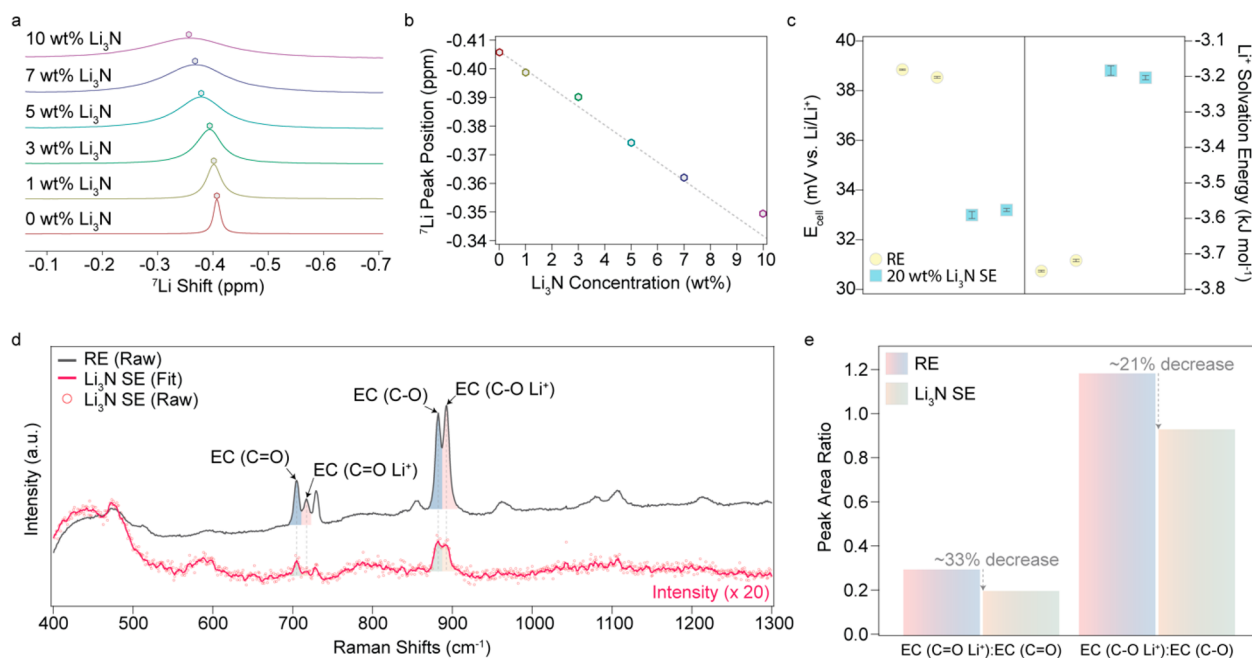


**Figure 3.**  $\text{Li}^+$  solvation environment of  $\text{Li}_3\text{N}$  SE. (a)  $^7\text{Li}$  NMR spectrum of 0–10 wt %  $\text{Li}_3\text{N}$  in RE.  $^7\text{Li}$  NMR peaks for the corresponding weight content of  $\text{Li}_3\text{N}$  in RE are indicated by the hexagonal symbols. (b)  $^7\text{Li}$  NMR peak positions based on 0–10 wt %  $\text{Li}_3\text{N}$  in RE. The dashed gray line represents the linear fit of the peaks. (c) The cell potential ( $E_{\text{cell}}$ ) and  $\text{Li}^+$  solvation energy measurements for RE and 20 wt %  $\text{Li}_3\text{N}$  SE. Two measurements were taken for each of the electrolytes. The averaged  $E_{\text{cell}}$  and solvation energy values with standard errors for RE (1st measurement:  $38.850 \pm 0.024$  mV vs  $\text{Li}/\text{Li}^+ | -3.748 \pm -0.002$  kJ mol $^{-1}$  and 2nd measurement:  $38.540 \pm 0.037$  mV vs  $\text{Li}/\text{Li}^+ | -3.719 \pm -0.003$  kJ mol $^{-1}$ ) and 20 wt %  $\text{Li}_3\text{N}$  SE (1st measurement:  $32.992 \pm 0.139$  mV vs  $\text{Li}/\text{Li}^+ | -3.183 \pm -0.013$  kJ mol $^{-1}$  and 2nd measurement:  $33.197 \pm 0.061$  mV vs  $\text{Li}/\text{Li}^+ | -3.203 \pm -0.006$  kJ mol $^{-1}$ ) were obtained by recording the measurements up to 3 s after the cell potentials were stabilized. (d) Raman spectrum for RE and  $\text{Li}_3\text{N}$  SE. Four major peaks were assigned for EC (C=O), EC (C=O  $\text{Li}^+$ ), EC (C–O), and EC (C–O  $\text{Li}^+$ ). (e) Raman peak area ratios of RE and  $\text{Li}_3\text{N}$  SE for EC (C=O):EC (C=O  $\text{Li}^+$ ) and EC (C–O):EC (C–O  $\text{Li}^+$ ) retrieved from (d).

formed at the  $\text{Li}^0/\text{Li}_3\text{N}$  interface can be depicted as the current collector ( $\text{Li}^0$  as the electron conductor) and solid electrolyte ( $\text{Li}_3\text{N}$  as the  $\text{Li}^+$  conductor) model, in which the charge transfers occurring at the heterojunction allow electro-deposition of  $\text{Li}^0$  on the surfaces of  $\text{Li}_3\text{N}$ . Hence, the  $J_0$  measurement substantiates the  $\text{Li}^0$  electrodeposition at the  $\text{Li}^0/\text{Li}_3\text{N}$  heterojunction (as observed in Figure 1d,e) by electrochemically probing the  $\text{Li}^0$ - $\text{Li}_3\text{N}$  interaction. We note that this outcome was particularly crucial as this serves as the first demonstration that  $J_0$  can also be impacted by the suspension electrolyte design, meaning the  $J_0$  of a particular liquid electrolyte can still be modified without changing the liquid components.

Since lower surface area and more compact  $\text{Li}^0$  electro-deposition morphologies indicate high CE and low Li nucleation overpotential,<sup>1,40,41</sup> CE and Li nucleation overpotential were measured from Li/Cu cells with RE and  $\text{Li}_3\text{N}$  SE to cross-validate the features attained from Figure 1c–f (Figure 1j,k). Figure 1j shows the representative voltage profiles of CE and Li nucleation overpotential measurements for RE and  $\text{Li}_3\text{N}$  SE. From the voltage profile analyses, it is apparent that  $\text{Li}_3\text{N}$  SE exhibited a higher CE and lower Li nucleation barrier than those of RE. Moreover, the inset of Figure 1j showed reduced overpotentials for  $\text{Li}_3\text{N}$  SE, suggesting facilitated  $\text{Li}^+$  transport. Duplicate measurements were taken with three identical Li/Cu cells containing each of the electrolytes to calculate averaged CE ( $97.48\% \pm 0.31\%$  for  $\text{Li}_3\text{N}$  SE and  $93.01\% \pm 2.21\%$  for RE) and Li nucleation overpotentials ( $56.43$  mV  $\pm 5.31$  mV for  $\text{Li}_3\text{N}$  SE and  $88.77$  mV  $\pm 5.11$  mV for RE) with standard errors (Figure 1k). Based on the

morphological and electrochemical analyses from Figure 1c–k, three noticeable features of  $\text{Li}_3\text{N}$  were observed: (i) guided  $\text{Li}^0$  electrodeposition along the surface of  $\text{Li}_3\text{N}$ , (ii) existence of  $\text{Li}^0$ - $\text{Li}_3\text{N}$  interaction in  $\text{Li}_3\text{N}$  SE, (iii) improved electrochemical performance of  $\text{Li}^0$  anodes, and (iv) facilitated  $\text{Li}^+$  transport with  $\text{Li}_3\text{N}$  in the liquid electrolyte.

**Analyses of  $\text{Li}_3\text{N}$  via First-Principles Calculations.** To construe the guided  $\text{Li}^0$  electrodeposition along the surfaces of  $\text{Li}_3\text{N}$  (Figure 1d,e), binding energies and diffusion barriers were computed for  $\text{Li}_3\text{N}$  via density functional theory (DFT). Based on X-ray powder diffraction (XRD) of  $\text{Li}_3\text{N}$ , four orientations were found: (001), (100), (002), and (110), of which (001) was the dominant surface of  $\text{Li}_3\text{N}$  (Figure S2). To relatively compare Li adatom binding energies and diffusion barrier of  $\text{Li}_3\text{N}$ , the same analyses were executed with  $\text{Li}^0$  (110) as (110) surface is most commonly observed for  $\text{Li}^0$  anodes.<sup>34,43</sup> Figure 2a shows thermodynamically favorable Li adatom binding sites on  $\text{Li}^0$  (110),  $\text{Li}_3\text{N}$  (001)|(002),  $\text{Li}_3\text{N}$  (110), and  $\text{Li}_3\text{N}$  (100) surfaces with the corresponding binding energies of  $-1.59$  eV,  $-3.44$  eV,  $-1.78$  eV, and  $-1.44$  eV, respectively (Figure 2b). The Li adatom binding energy trend in Figure 2b suggests that  $\text{Li}_3\text{N}$  (001)|(002) surfaces (please note that the (002) surface is equivalent to the (001) surface of  $\text{Li}_3\text{N}$ ) were the most favorable Li adatom binding surfaces. This means that Li thermodynamically prefers to get adsorbed onto  $\text{Li}_3\text{N}$  (001)|(002) surfaces instead of the  $\text{Li}^0$  (110) surface. The favored Li adsorption onto  $\text{Li}_3\text{N}$  surfaces further justifies the change in  $J_0$  observed for  $\text{Li}_3\text{N}$  SE (Figure 1i), as the DFT results (Figure 2b) indicate that it is thermodynamically more favorable for Li to

bind with  $\text{Li}_3\text{N}$  rather than with  $\text{Li}^0$ . Thereby, the results in Figure 2b rationalize the  $\text{Li}^0$ - $\text{Li}_3\text{N}$  interaction, illustrating favored Li growth at the  $\text{Li}^0/\text{Li}_3\text{N}$  heterojunction. Additionally, the binding energies of  $\text{Li}_3\text{N}$  (001)|(002) surfaces were significantly higher, about two folds, than that of  $\text{Li}^0$  (110),  $\text{Li}_3\text{N}$  (110), and  $\text{Li}_3\text{N}$  (100) surfaces, in which the binding energies of  $\text{Li}_3\text{N}$  (110) and (100) were comparable to that of  $\text{Li}^0$  (110). Since the  $\text{Li}_3\text{N}$  (001) surface was experimentally found to be the primary surface (Figure S2),<sup>34,43</sup> this supports the claim that  $\text{Li}_3\text{N}$ , specifically  $\text{Li}_3\text{N}$  (001)|(002) surfaces, is lithiophilic, which explains the guided  $\text{Li}^0$  electrodeposition along the surfaces of  $\text{Li}_3\text{N}$ .

With the aim of further supporting the stabilized  $\text{Li}^0$  electrodeposition with  $\text{Li}_3\text{N}$ , the surface diffusion barrier of Li adatom on the  $\text{Li}_3\text{N}$  (001) surface was calculated as the low diffusion barrier which facilitates surface diffusion of Li to promote uniform  $\text{Li}^0$  electrodeposition (Figure 2c).<sup>43–45</sup> In Figure 2c, Li was diffusing from the nitrogen to the adjacent nitrogen. From this diffusion trajectory, a total of eight relative energies, which represent threshold energies needed to adsorb Li adatom across the diffusion pathway, were computed to figure out the diffusion barrier. The diffusion barrier of Li adatom on  $\text{Li}_3\text{N}$  (001) surface was 0.133 eV (Figure 2d). Then, the diffusion barrier of  $\text{Li}_3\text{N}$  (0.133 eV) was compared with other prominent SEI inorganic compounds, such as  $\text{Li}_2\text{O}$  (0.319 eV),  $\text{Li}_2\text{CO}_3$  (0.232 eV), LiF (0.169 eV), and LiOH (0.141 eV), to comparatively understand the diffusion barrier for  $\text{Li}_3\text{N}$ .<sup>44</sup> According to Figure 2e,  $\text{Li}_3\text{N}$  has the lowest diffusion barrier, claiming  $\text{Li}_3\text{N}$  as the most favorable SEI inorganic in terms of Li surface diffusion characteristics. We note that the low diffusion barrier would be an important parameter for ionically conductive inorganics, such as  $\text{Li}_3\text{N}$ , stabilizing the  $\text{Li}^0$  electrodeposition at the  $\text{Li}^0$ /inorganic heterojunction. Furthermore, the surface energy of  $\text{Li}_3\text{N}$  (001) surface (3.60 meV  $\text{atom}^{-1} \text{ \AA}^{-2}$ ) was higher than that of  $\text{Li}^0$  (110) surface (2.58 meV  $\text{atom}^{-1} \text{ \AA}^{-2}$ ), in which the higher surface energy of  $\text{Li}_3\text{N}$  at the  $\text{Li}^0/\text{Li}_3\text{N}$  heterojunction suppresses dendritic  $\text{Li}^0$  growth (Figure S3).<sup>46</sup> Hence, the high binding energy, low diffusion barrier, and high surface energy of  $\text{Li}_3\text{N}$  support the observed guided and stabilized  $\text{Li}^0$  electrodeposition along the surface of  $\text{Li}_3\text{N}$  observed in Figure 1d,e and Figure S1.

**$\text{Li}^+$  Solvation Environment of  $\text{Li}_3\text{N}$ .**  $^7\text{Li}$  nuclear magnetic resonance (NMR), relative  $\text{Li}^+$  solvation energy, and Raman analyses were performed to investigate the  $\text{Li}^+$  solvation environment influenced by  $\text{Li}_3\text{N}$  in the electrolyte (Figure 3). Figure 3a shows  $^7\text{Li}$  NMR spectra of RE (0 wt %  $\text{Li}_3\text{N}$ ) and  $\text{Li}_3\text{N}$  SE (1–10 wt %  $\text{Li}_3\text{N}$  in RE).  $^7\text{Li}$  NMR peaks were shifted in the downfield direction, meaning the peaks were moving to the higher parts per million (ppm), as the  $\text{Li}_3\text{N}$  content increased. The peak shifts directly reflect the changes in the  $\text{Li}^+$  solvation environment, in which the downfield peak shifts signify decreased electron density around the nuclei of solvated  $\text{Li}^+$  in the electrolyte.<sup>47</sup> As the solid particles in the liquid sample agitate the magnetic field during the NMR measurement, the retrieved signals become heterogeneous, which broadens the  $^7\text{Li}$  NMR peak. This means that the peak becomes broader as the suspension concentration increases as shown in Figure 3a. Despite the peak broadening as a function of suspension content, all the peak shapes are symmetric, which confirms that the peak position is shifting with respect to the changes in the suspension content. To verify the  $^7\text{Li}$  shift stems from dissociated  $\text{Li}^+$  from  $\text{LiPF}_6$ , not  $\text{Li}_3\text{N}$ , the  $^7\text{Li}$

NMR spectrum of RE without  $\text{LiPF}_6$ , supernatant of  $\text{Li}_3\text{N}$  SE without  $\text{LiPF}_6$ , and  $\text{Li}_3\text{N}$  SE without  $\text{LiPF}_6$  were measured (Figure S4). The spectra in Figure S4 do not exhibit any peaks, meaning that the dissociated  $\text{Li}^+$  from  $\text{Li}_3\text{N}$  was too low to be detected by the  $^7\text{Li}$  NMR. Therefore, the  $^7\text{Li}$  shift observed in Figure 3a is due to the change in the electron density of dissociated  $\text{Li}^+$  nuclei from  $\text{LiPF}_6$ , validating that  $\text{Li}_3\text{N}$  is modifying the solvation environment of  $\text{Li}^+$  in the suspension electrolyte. The downfield peak shifts observed in Figure 3a illustrate that the solvated  $\text{Li}^+$  in  $\text{Li}_3\text{N}$  SE became less coordinated with solvating electrolyte species. Since the peak position varied with respect to the  $\text{Li}_3\text{N}$  contents, the peak positions were plotted in Figure 3b. The peak positions as a function of the  $\text{Li}_3\text{N}$  content were almost linear up to 7 wt %. Then above 7 wt %  $\text{Li}_3\text{N}$ , the peak shift was less in magnitude. Based on the suspension electrolyte design, the dispersity of the suspension also matters to obtain reliable electrochemical performance. Despite the  $^7\text{Li}$  downfield peak shift observed for 10 wt %  $\text{Li}_3\text{N}$  in Figure 3b, particle aggregation above 7 wt % was observed (see Figure S4). Since the  $^7\text{Li}$  peak shift depends on the surface area to volume ratio<sup>6</sup> of the  $\text{Li}_3\text{N}$  suspension, Figure 3b correctly shows that the peak shift becomes nonlinear and shifts less above 7 wt %, indicating that the suspension starts to aggregate (reducing the surface area to volume ratio of the suspension) as observed in Figure S5. Hence, 7 wt %  $\text{Li}_3\text{N}$  content was used to analyze the electrochemical performance, as this weight content was the most reliable for making  $\text{Li}_3\text{N}$  SE. Please note that optimizing the suspension content for the suspension electrolytes depends on several parameters (i.e., suspension types, dimensions, geometries, electrolyte formulations, and so on), in which the reported optimized content can be changed when the parameters vary.

To further support the changes in the  $\text{Li}^+$  solvation environment of  $\text{Li}_3\text{N}$ , relative  $\text{Li}^+$  solvation energies were potentiometrically probed for RE and 20 wt %  $\text{Li}_3\text{N}$  SE. With symmetric  $\text{Li}^0$  electrodes and asymmetric electrolytes configured in H-cell, it became possible to electrochemically measure the relative  $\text{Li}^+$  solvation energies of electrolytes (Figure 3c).<sup>11</sup> The reason for the high weight content of  $\text{Li}_3\text{N}$  used in the  $\text{Li}^+$  solvation energy measurement was to vividly observe the direction of the  $\text{Li}^+$  solvation energy change for  $\text{Li}_3\text{N}$  SE. From Figure 3c, 20 wt %  $\text{Li}_3\text{N}$  SE exhibited lower cell potential ( $E_{\text{cell}}$ ) and more positive  $\text{Li}^+$  solvation energy than those of RE. These results were critical as the lower  $E_{\text{cell}}$  and higher  $\text{Li}^+$  solvation energy cross-check the changes in the  $\text{Li}^+$  solvation environment with  $\text{Li}_3\text{N}$  in the electrolyte as observed from  $^7\text{Li}$  NMR measurements (Figure 3a).<sup>6,11</sup> Also, the lower  $E_{\text{cell}}$  and higher  $\text{Li}^+$  solvation energy of 20 wt %  $\text{Li}_3\text{N}$  SE translate to the weakly solvating  $\text{Li}^+$  environment.<sup>11</sup> This interchangeably means that the interaction between solvated  $\text{Li}^+$  and solvating electrolyte species has been weakened by the presence of  $\text{Li}_3\text{N}$  in the electrolyte, which agrees with  $^7\text{Li}$  NMR analysis in Figure 3a. Thereby, we concluded that  $\text{Li}_3\text{N}$  in the electrolyte modifies  $\text{Li}^+$  solvation environment by decreasing the interaction between  $\text{Li}^+$  and solvating electrolyte species, which creates a weakly solvating environment. Also, it is worth mentioning that the weakly solvating environment allows facilitated  $\text{Li}^0$  electrodeposition and  $\text{Li}^+$  desolvation kinetics, demonstrating beneficial features of  $\text{Li}_3\text{N}$ .<sup>42</sup>

To verify the decreased interaction between  $\text{Li}^+$  and the solvating electrolyte species observed in  $^7\text{Li}$  NMR and the relative  $\text{Li}^+$  solvation energy analyses in Figure 3a–c, Raman

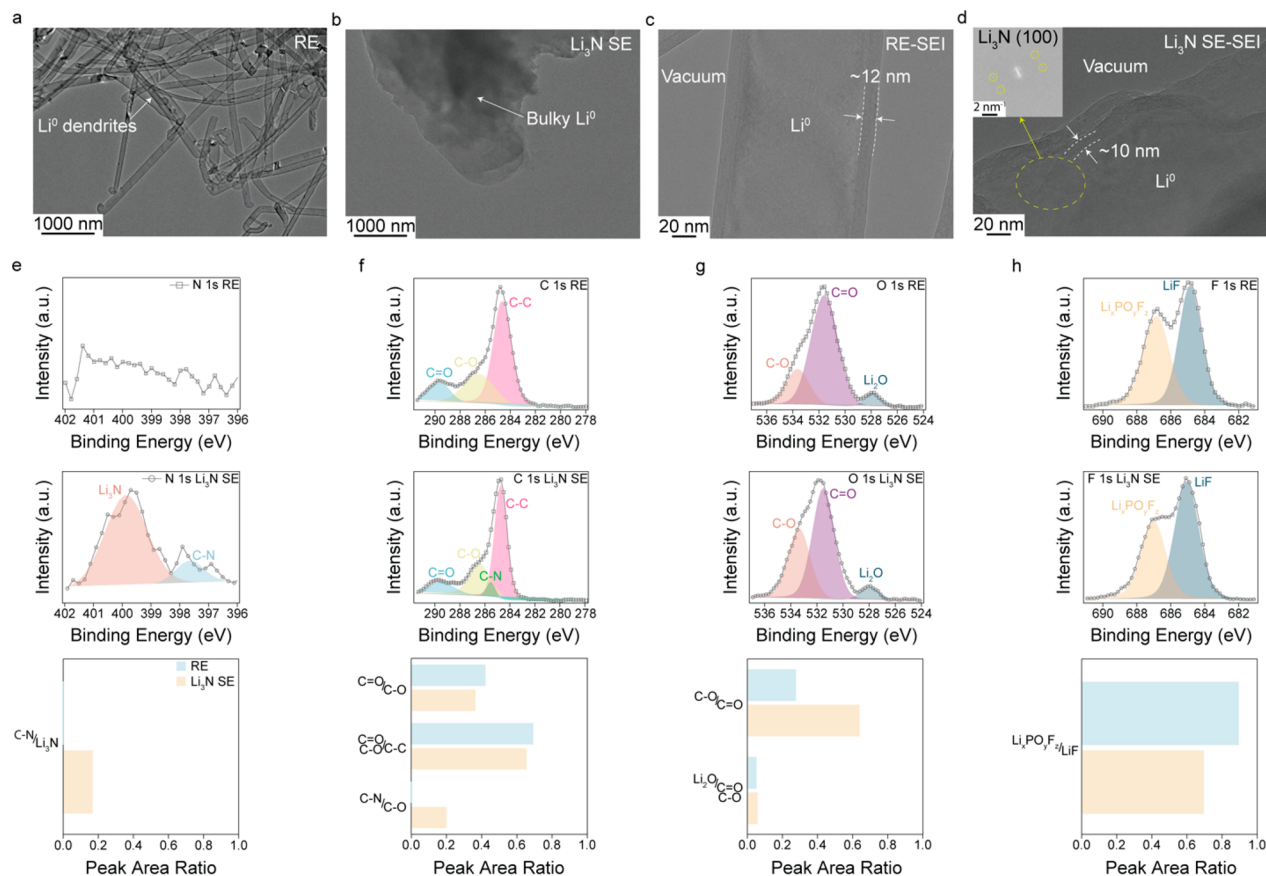


**Figure 4.**  $\text{Li}^0$  interphases with RE and  $\text{Li}_3\text{N}$  SE. (a) A low magnification cryo-TEM image of  $\text{Li}^0$  electrodeposits on Cu TEM grid with RE. The arrow indicates dendritic  $\text{Li}^0$  electrodeposits with RE. (b) A low magnification cryo-TEM image of  $\text{Li}^0$  electrodeposits on Cu TEM grid with  $\text{Li}_3\text{N}$  SE. The arrow indicates bulky  $\text{Li}^0$  electrodeposits with  $\text{Li}_3\text{N}$  SE. (c) A high magnification cryo-TEM image of  $\text{Li}^0$  dendrite and RE-SEI, indicated by the arrows. (d) A high magnification cryo-TEM image of bulky  $\text{Li}^0$  and  $\text{Li}_3\text{N}$  SE-SEI, indicated by the arrows. The inset shows the fast Fourier transform pattern of the image. From the inverse fast Fourier transform of the inset, the dashed yellow circle indicates the position of  $\text{Li}_3\text{N}$  lattice. (e) N 1s XPS spectra of 1 mAh  $\text{cm}^{-2}$  electrodeposited  $\text{Li}^0$  on Cu at 1 mA  $\text{cm}^{-2}$  from Li/Cu cells with RE and  $\text{Li}_3\text{N}$  SE. The bottom plot represents the peak area ratio of C-N: $\text{Li}_3\text{N}$  based on N 1s XPS spectra of RE and  $\text{Li}_3\text{N}$  SE. (f) C 1s XPS spectra of 1 mAh  $\text{cm}^{-2}$  electrodeposited  $\text{Li}^0$  on Cu at 1 mA  $\text{cm}^{-2}$  from Li/Cu cells with RE and  $\text{Li}_3\text{N}$  SE. The bottom plot represents the peak area ratio of C=O:C-O, C=O C-O:C-C, and C-N:C-O based on C 1s XPS spectra of RE and  $\text{Li}_3\text{N}$  SE. (g) O 1s XPS spectra of 1 mAh  $\text{cm}^{-2}$  electrodeposited  $\text{Li}^0$  on Cu at 1 mA  $\text{cm}^{-2}$  from Li/Cu cells with RE and  $\text{Li}_3\text{N}$  SE. The bottom plot represents the peak area ratio of C-O:C=O and  $\text{Li}_2\text{O}$ :C=O C-O based on O 1s XPS spectra of RE and  $\text{Li}_3\text{N}$  SE. (h) F 1s XPS spectra of 1 mAh  $\text{cm}^{-2}$  electrodeposited  $\text{Li}^0$  on Cu at 1 mA  $\text{cm}^{-2}$  from Li/Cu cells with RE and  $\text{Li}_3\text{N}$  SE. The bottom plot represents the peak area ratio of  $\text{Li}_x\text{PO}_y\text{F}_z$ :LiF based on F 1s XPS spectra of RE and  $\text{Li}_3\text{N}$  SE.

spectra of RE and  $\text{Li}_3\text{N}$  SE were examined to understand  $\text{Li}^+$  to solvent coordination (Figure 3d). Due to the solid nanoparticles in the liquid electrolyte ( $\text{Li}_3\text{N}$  SE), the retrieved intensity for  $\text{Li}_3\text{N}$  SE was relatively lower than that for RE. Despite the low signal, reliable peaks for alkoxy, EC (C-O), and carbonyl, EC (C=O), groups for EC were observed for  $\text{Li}_3\text{N}$  SE (Figure 3d). The peaks around 892  $\text{cm}^{-1}$ , 882  $\text{cm}^{-1}$ , 718  $\text{cm}^{-1}$ , and 705  $\text{cm}^{-1}$  represent solvated alkoxy groups of EC with  $\text{Li}^+$ , EC (C-O  $\text{Li}^+$ ), nonsolvated alkoxy groups of EC, EC (C-O), solvated carbonyl groups of EC with  $\text{Li}^+$ , EC (C=O  $\text{Li}^+$ ), and nonsolvated carbonyl groups of EC, EC (C=O), respectively.<sup>48,49</sup> To qualitatively compare the  $\text{Li}^+$ -EC coordination between RE and  $\text{Li}_3\text{N}$  SE, the corresponding peaks were integrated and normalized to investigate the relative  $\text{Li}^+$ -EC coordination, which was denoted as the EC (C=O  $\text{Li}^+$ ):EC (C=O) and EC (C-O  $\text{Li}^+$ ):EC (C-O) ratios. By calculating the peak area ratios in Figure 3e, the decrease in  $\text{Li}^+$ -EC coordination was clearly observed for  $\text{Li}_3\text{N}$  SE, in which both EC (C=O  $\text{Li}^+$ ):EC (C=O) and EC (C-O  $\text{Li}^+$ ):EC (C-O) ratios for  $\text{Li}_3\text{N}$  SE showed approximately 33% and 21% relative

decrease compared to those for RE. The decrease in  $\text{Li}^+$ -EC coordination for  $\text{Li}_3\text{N}$  SE cross-validates the results from  $^7\text{Li}$  NMR (the decrease in electron density around the nuclei of solvated  $\text{Li}^+$  in  $\text{Li}_3\text{N}$  SE) and the relative  $\text{Li}^+$  solvation energy (weakly solvating  $\text{Li}^+$  environment for  $\text{Li}_3\text{N}$  SE) measurements. Thusly, these results reveal the essential roles of  $\text{Li}_3\text{N}$  in terms of the  $\text{Li}^+$  solvation environment:  $\text{Li}_3\text{N}$  changes  $\text{Li}^+$  solvation environment by decreasing the interaction between  $\text{Li}^+$  and solvating electrolyte species, and specifically  $\text{Li}_3\text{N}$  weakens the  $\text{Li}^+$ -solvent coordination that induces the weakly solvating environment in the electrolyte.

**Analyses of  $\text{Li}^0$  Interphase.**  $\text{Li}^0$  electrodeposition morphologies and SEIs with RE and  $\text{Li}_3\text{N}$  SE were investigated via cryogenic transmission electron microscopy (cryo-TEM) to consolidate observed features of  $\text{Li}_3\text{N}$  in Figures 1–3 (Figure 4a–d). With RE, dendritic  $\text{Li}^0$  electrodeposition morphology was observed (Figure 4a), as seen in Figure 1c. On the contrary, a bulky  $\text{Li}^0$  electrodeposit was observed with  $\text{Li}_3\text{N}$  SE (Figure 4b), indicating a more compact  $\text{Li}^0$  electrodeposition with  $\text{Li}_3\text{N}$  in the electrolyte (Figure 1d,e and Figure S1). To

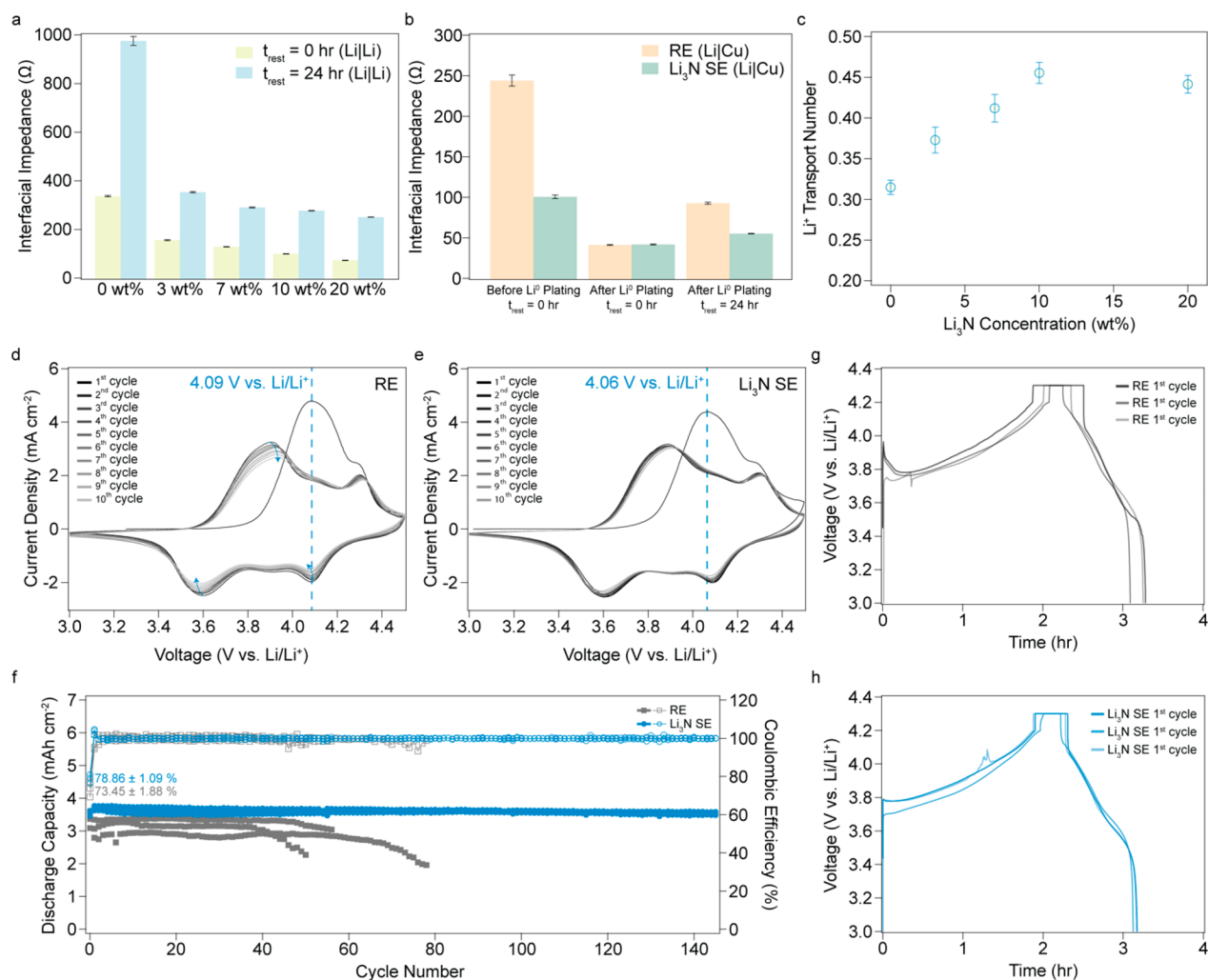


**Figure 5.** Electrochemical characteristics of  $\text{Li}_3\text{N}$  SE for  $\text{Li}^0$  anodes. (a) Measured interfacial impedances from  $\text{Li|Li}$  cells with 0–20 wt %  $\text{Li}_3\text{N}$  in RE with respect to the aging time ( $t_{\text{rest}} = 0$  and 24 h). Three identical  $\text{Li|Li}$  cells were used for each electrolyte to obtain the averaged interfacial impedances with standard errors. (b) Measured interfacial impedances from  $\text{Li|Cu}$  cells at  $t_{\text{rest}} = 0$  h and after  $\text{Li}^0$  electrodeposited on Cu at  $t_{\text{rest}} = 0$  and 24 h with RE and  $\text{Li}_3\text{N}$  SE. Three identical  $\text{Li|Cu}$  cells were used for each condition to obtain the averaged interfacial impedances with standard errors. The current density of  $1 \text{ mA cm}^{-2}$  and capacity of  $1 \text{ mAh cm}^{-2}$  were used for plating  $\text{Li}^0$ . (c)  $\text{Li}^+$  transport number measured from  $\text{Li|Li}$  cells with 0–20 wt %  $\text{Li}_3\text{N}$  in RE. Three identical  $\text{Li|Li}$  cells were used for each electrolyte to obtain the averaged  $\text{Li}^+$  transport number with standard errors. (d) First 10 cycle cyclic voltammograms of the  $\text{Li|Li}_1\text{Ni}_{0.8}\text{Co}_{0.1}\text{Mn}_{0.1}$  cell with RE. The voltage window and scan rate used are 3.0 to 4.5 V vs  $\text{Li/Li}^+$  and  $0.1 \text{ mV s}^{-1}$ . The dashed line indicates the peak position during the first charge cycle of the  $\text{Li|Li}_1\text{Ni}_{0.8}\text{Co}_{0.1}\text{Mn}_{0.1}$  cell. The arrows represent the voltage hysteresis during the cell cycling. (e) First 10 cycle cyclic voltammograms of the  $\text{Li|Li}_1\text{Ni}_{0.8}\text{Co}_{0.1}\text{Mn}_{0.1}$  cell with  $\text{Li}_3\text{N}$  SE. The voltage window and scan rate used are 3.0 to 4.5 V vs  $\text{Li/Li}^+$  and  $0.1 \text{ mV s}^{-1}$ . The dashed line indicates the peak position during the first charge cycle of the  $\text{Li|Li}_1\text{Ni}_{0.8}\text{Co}_{0.1}\text{Mn}_{0.1}$  cell. (f) Cycling profiles of  $\text{Li|Li}_1\text{Ni}_{0.8}\text{Co}_{0.1}\text{Mn}_{0.1}$  cells with RE and  $\text{Li}_3\text{N}$  SE. The filled and open symbols represent discharge capacity and CE. The cell cycling was performed using 0.5C charging (0.5C) and 1C discharging (1D) with the voltage window of 3.0–4.3 V vs  $\text{Li/Li}^+$ . Three identical  $\text{Li|NMC811}$  cells were measured with RE and  $\text{Li}_3\text{N}$  SE, and the averaged first cycle CE with each electrolyte is shown with the standard error. (g) The first cycle voltage profiles of  $\text{Li|Li}_1\text{Ni}_{0.8}\text{Co}_{0.1}\text{Mn}_{0.1}$  cells with RE. (h) The first cycle voltage profiles of  $\text{Li|Li}_1\text{Ni}_{0.8}\text{Co}_{0.1}\text{Mn}_{0.1}$  cells with  $\text{Li}_3\text{N}$  SE.

look closely into the SEIs on  $\text{Li}^0$  with RE (RE-SEI) and  $\text{Li}_3\text{N}$  SE ( $\text{Li}_3\text{N}$  SE-SEI), the thickness of RE-SEI (Figure 4c) and  $\text{Li}_3\text{N}$  SE-SEI (Figure 4d) was estimated with the high magnification cryo-TEM images. The measured SEI thicknesses of RE-SEI and  $\text{Li}_3\text{N}$  SE-SEI were about 12 and 10 nm. Furthermore, the fast Fourier transform (FFT) pattern in the Figure 4d inset exhibits the lattice of  $\text{Li}_3\text{N}$ , indicating the presence of  $\text{Li}_3\text{N}$  in the  $\text{Li}^0$  electrodeposits. From the inverse FFT of the Figure 4d inset, the observed  $\text{Li}_3\text{N}$  lattice was mapped in Figure S6 for visualization, in which the detected  $\text{Li}_3\text{N}$  lattice spot is demarcated by a dashed yellow circle in Figure 4d. Therefore, embedded  $\text{Li}_3\text{N}$  into the  $\text{Li}^0$  electrodeposit was found for  $\text{Li}_3\text{N}$  SE, in which the presence of

embedded  $\text{Li}_3\text{N}$  in  $\text{Li}^0$  electrodeposits further confirmed guided  $\text{Li}^0$  electrodeposition behavior along the  $\text{Li}_3\text{N}$  surface as observed in SEM (Figure 1d,e) and DFT (Figure 2) analyses.

X-ray photoelectron spectroscopy (XPS) was performed to analyze chemistries of  $\text{Li}^0$  interphases formed by RE and  $\text{Li}_3\text{N}$  SE (Figure 4e–h). Based on N 1s narrow XPS scans,  $\text{Li}_3\text{N}$  and C–N were detected on the  $\text{Li}^0$  interphase derived from  $\text{Li}_3\text{N}$  SE, whereas no N 1s signals were retrieved from the  $\text{Li}^0$  interphase derived from RE as RE contains no nitrogen species (Figure 4e). The existence of  $\text{Li}_3\text{N}$  can be explained by the guided  $\text{Li}^0$  electrodeposition along the surface of  $\text{Li}_3\text{N}$  that gets engulfed during the  $\text{Li}^0$  plating (Figure 1d,e, Figure S1, and

Figure 4d). We hypothesize that C–N bonds were formed during the reduction of solvent species at the interface junction between  $\text{Li}_3\text{N}$  and  $\text{Li}^0$ , at which the electrolyte should also be reduced at the surface of  $\text{Li}_3\text{N}$  due to the plating potential below 0 V vs  $\text{Li}/\text{Li}^+$ .<sup>3</sup> The ratio of C–N to  $\text{Li}_3\text{N}$  (C–N/ $\text{Li}_3\text{N}$ ) was calculated to understand which species were dominantly present at the  $\text{Li}^0$  interphase. The C–N/ $\text{Li}_3\text{N}$  ratio was around 0.18, indicating that  $\text{Li}_3\text{N}$  more dominantly existed at the  $\text{Li}^0$  interphase formed by  $\text{Li}_3\text{N}$  SE (Figure 4e). From C 1s narrow XPS scans (Figure 4f), there were three distinct differences observed between the  $\text{Li}^0$  interphase formed by RE and  $\text{Li}_3\text{N}$  SE: (i) a relative increase of C–O, (ii) lower C–C to C–O + C=O ratio (C–C/C–O C=O), and (iii) C–N species for the  $\text{Li}^0$  interphase of  $\text{Li}_3\text{N}$  SE. It has been found that enrichment of C–O (alkoxides and ethers) over C=O (carbonates) groups in the organic parts of the SEIs on  $\text{Li}^0$  provides improved passivity, enhanced  $\text{Li}^+$  transport, and physicochemical stability, implying beneficial features of C–O over C=O species in the SEIs.<sup>50–53</sup> Also, C=O + C–O over C–C ratio (C–O C=O/C–C) represents a relative solvent decomposition at the interphase of  $\text{Li}^0$  anodes, in which C–C and C–O C=O contents should increase and decrease, respectively, upon a more solvent decomposition and complete reduction of solvent molecules to form Li bound species from C–O and C=O groups.<sup>50–52</sup> The presence of C–N and the low C–N/C–O ratio in Figure 4f also cross-check the observed C–N in Figure 4e. Hence, the lower C=O/C–O and C=O C–O/C–C ratios for  $\text{Li}_3\text{N}$  SE than those for RE suggest a better SEI passivity and a less solvent decomposition on  $\text{Li}^0$  anodes. O 1s narrow XPS scans (Figure 4g), which exhibited higher C–O/C=O and  $\text{Li}_2\text{O}/\text{C=O}$  C–O ratios for  $\text{Li}_3\text{N}$  SE, showed the same aspects of  $\text{Li}^0$  interphase formed by  $\text{Li}_3\text{N}$  SE as observed in Figure 4f. Moreover, a lower  $\text{Li}_x\text{PO}_y\text{F}_z/\text{LiF}$  ratio for  $\text{Li}_3\text{N}$  SE than that for RE was observed from F 1s narrow XPS scans (Figure 4h). The lower  $\text{Li}_x\text{PO}_y\text{F}_z/\text{LiF}$  ratio for  $\text{Li}_3\text{N}$  SE indicates a reduced solvent decomposition as the oxygen in the  $\text{Li}_x\text{PO}_y\text{F}_z$  complex originates from the solvent decomposition with anions. To further verify the reduced solvent decomposition at the  $\text{Li}^0$  interphase of  $\text{Li}_3\text{N}$  SE, elemental ratios of P/C, F/C, and O/C were calculated (Figure S7). The lower P/C, F/C, and O/C ratios were achieved for  $\text{Li}_3\text{N}$  SE than those for RE, meaning reduced solvent-derived species for the  $\text{Li}^0$  interphase formed by  $\text{Li}_3\text{N}$  SE. Overall, XPS analyses manifest that less solvent decomposition and better  $\text{Li}^0$  interphase passivation characteristics were achieved with  $\text{Li}_3\text{N}$  SE. This also confirms the impact of the modified  $\text{Li}^+$  solvation environment by  $\text{Li}_3\text{N}$  as observed in Figure 3, in which the decrease in the  $\text{Li}^+$ -solvent coordination of solvated  $\text{Li}^+$  with  $\text{Li}_3\text{N}$  in the electrolyte suppressed solvent decomposition and promoted a complete solvent decomposition.

**Electrochemical Performance Analyses.** To understand the electrochemical properties of  $\text{Li}^0$  interphase formed by RE and  $\text{Li}_3\text{N}$  SE, interfacial impedances were measured for RE (0 wt %  $\text{Li}_3\text{N}$ ) and 3–20 wt %  $\text{Li}_3\text{N}$  SE from  $\text{LiLi}$  cells before and after aging<sup>16</sup> the cell for a day (Figure 5a, Figure S8, and Table S1). The interfacial impedances of  $\text{Li}^0$  with  $\text{Li}_3\text{N}$  SE electrolytes were much lower than that with RE, which can be expected from the weakly solvating environment and organic-poor  $\text{Li}^0$  interphase<sup>3</sup> with  $\text{Li}_3\text{N}$ . Also, the temporal characteristics of the interfacial impedance changes for  $\text{Li}_3\text{N}$  SE were more stable than that for RE. Moreover, the interfacial stability of electrodeposited  $\text{Li}^0$  with RE and  $\text{Li}_3\text{N}$  SE was

investigated by measuring the interfacial impedances before and after  $\text{Li}^0$  plating as well as aging the electrodeposited  $\text{Li}^0$  for a day from  $\text{LiCu}$  cells (Figure 5b, Figure S9, and Table S2). The magnitude of the interfacial impedance changes before and after  $\text{Li}^0$  plating as well as after aging was lower for  $\text{Li}_3\text{N}$  SE, demonstrating stable electrodeposition of  $\text{Li}^0$  with and temporally stabilized  $\text{Li}^0$  interphase formed by  $\text{Li}_3\text{N}$  SE. The altered  $\text{Li}^+$  solvation environment with  $\text{Li}_3\text{N}$  in the electrolyte contributes to the stabilized temporal characteristics of  $\text{Li}^0$  interphase with  $\text{Li}_3\text{N}$  SE, as the decrease in  $\text{Li}^+$ -solvent interaction helps to create organic-poor SEI that mitigates SEI swelling.<sup>3,15</sup> Remarkably, the  $\text{Li}^+$  transport number of  $\text{Li}_3\text{N}$  SE increased with the presence of  $\text{Li}_3\text{N}$  in the electrolyte (Figure 5c and Table S3). Having a higher  $\text{Li}^+$  transport number can reduce the overpotential, as a larger fraction of the applied current is getting used to migrate  $\text{Li}^+$ . To cross-validate the effect of the improved  $\text{Li}^+$  transport number, the ionic conductivity was measured for RE ( $0.272 \pm 0.008 \text{ mS cm}^{-1}$ ) and  $\text{Li}_3\text{N}$  SE ( $0.261 \pm 0.013 \text{ mS cm}^{-1}$ ), see Figure S10. The ionic conductivities of RE and  $\text{Li}_3\text{N}$  SE were comparable to each other, indicating that the improved  $\text{Li}^+$  transport number with  $\text{Li}_3\text{N}$  SE enables reducing the cell overpotential as the electrolyte conductivity remains similar for RE and  $\text{Li}_3\text{N}$  SE. Accordingly, the decrease in interfacial impedance, increase in  $\text{Li}^+$  transport number, and no change in electrolyte ionic conductivity justify the reduced  $\text{Li}^0$ -plating/stripping cell overpotential with  $\text{Li}_3\text{N}$  SE, as observed in Figure 1j.

To verify the electrochemical activity of  $\text{Li}_3\text{N}$  in  $\text{Li}_3\text{N}$  SE, cyclic voltammetry scans (from 3 to 4.5 V vs  $\text{Li}/\text{Li}^+$ ) and linear sweep voltammetry (LSV, from 3 to 5 V vs  $\text{Li}/\text{Li}^+$ ) were performed with  $\text{LiLi}_1\text{Ni}_{0.8}\text{Co}_{0.1}\text{Mn}_{0.1}$  and  $\text{LiAl}$  cells (Figure 5d,e, Figure S11, and Figure S12). By comparing the representative cyclic voltammograms of  $\text{LiLi}_1\text{Ni}_{0.8}\text{Co}_{0.1}\text{Mn}_{0.1}$  cells with RE (Figure 5d) and  $\text{Li}_3\text{N}$  SE (Figure 5e), a lower first charging redox potential and less cyclic voltammogram hysteresis,<sup>43,54</sup> signifying facilitated  $\text{Li}^+$  transport and reversible redox reactions in the full cell with  $\text{Li}_3\text{N}$  SE, were observed for  $\text{Li}_3\text{N}$  SE than those for RE. Additional cyclic voltammograms are shown in Figure S11. LSV measurements in Figure S12 revealed that the  $\text{Li}_3\text{N}$  in the electrolyte remains electrochemically stable as no current overshoot was observed. Also, the cyclic voltammograms of  $\text{LiLiNMC811}$  with  $\text{Li}_3\text{N}$  SE in Figure 5e did not exhibit additional redox peaks up to 4.5 V vs  $\text{Li}/\text{Li}^+$ . We hypothesize that oxidizing dispersed  $\text{Li}_3\text{N}$  in the liquid electrolyte may require a higher voltage to oxidize  $\text{Li}_3\text{N}$  as the surfaces of  $\text{Li}_3\text{N}$  are well-wetted by the liquid electrolyte, which can hinder direct contact of dispersed  $\text{Li}_3\text{N}$  with the cathode materials. To confirm the cycling characteristics of  $\text{LiLi}_1\text{Ni}_{0.8}\text{Co}_{0.1}\text{Mn}_{0.1}$  full cells with RE and  $\text{Li}_3\text{N}$  SE, cycling and corresponding voltage profiles are illustrated in Figure 5f–h. The full cells with  $\text{Li}_3\text{N}$  SE yielded prolonged cycle life with a higher first cycle CE (Figure 5f). By comparing the first cycle voltage profiles of RE (Figure 5g) and  $\text{Li}_3\text{N}$  SE (Figure 5h) retrieved from Figure 5f, a smaller voltage overshoot at the beginning of the first charging was observed for the  $\text{Li}_3\text{N}$  SE, demonstrating better  $\text{Li}^+$  transport and stabilized electrochemical reactions in the full cells.

## CONCLUSIONS

By combining empirical and first-principles calculation analyses of  $\text{Li}_3\text{N}$  SE, we showed that  $\text{Li}_3\text{N}$  guides  $\text{Li}^0$  electrodeposition along its surface via thermodynamically favored  $\text{Li}^0$ - $\text{Li}_3\text{N}$  interactions, creates the weakly solvating  $\text{Li}^+$  environment by

decreasing the interaction between  $\text{Li}^+$  and solvating electrolyte species, suppresses solvent decomposition on  $\text{Li}^0$  anodes, induces organic-poor SEI on  $\text{Li}^0$  anodes, facilitates  $\text{Li}^+$  transport in the electrolyte, and promotes reversible electrochemical reactions in the full cells. The outcome of this study can potentially serve as one of the scientific guidelines (i.e., inorganics that promote the weakly solvating  $\text{Li}^+$  environment) to rationalize the roles played by inorganic compounds in the SEIs on  $\text{Li}^0$  anodes. Importantly, it is crucial to realize that SEIs on  $\text{Li}^0$  anodes are still electrolyte permeable, as evidenced by SEI swelling properties,<sup>15</sup> in which solvated  $\text{Li}^+$  electrolyte species are present within the SEI layer. Therefore, we must understand how the  $\text{Li}^+$  solvation environment is influenced and controlled by SEI inorganic species at the SEI/ $\text{Li}^0$  interface that dictates  $\text{Li}^+$  transport as well as charge transfer behavior and impacts SEI evolution on  $\text{Li}^0$  anodes. We believe that the systematic revealment of SEI inorganic features would ultimately allow sophisticated electrolyte engineering strategies that contribute to designing high-performance SEIs on  $\text{Li}^0$  anodes for realizing reliable yet practical energy-dense LMBs.

## METHODS

**Materials.** The electrolytes were prepared and handled in an Ar-filled glovebox with an  $\text{O}_2$  concentration below 0.2 ppm and  $\text{H}_2\text{O}$  concentration below 0.01 ppm. The reference electrolyte (RE) was made with 1 M  $\text{LiPF}_6$  in EC:DEC (1:1 v/v) (Gotion LP40) with 10 vol % FEC (Gotion). The  $\text{Li}_3\text{N}$  suspension electrolyte ( $\text{Li}_3\text{N}$  SE) was prepared by mixing indicated amount (3–20 wt %) of  $\text{Li}_3\text{N}$  nanoparticles (80–100 nm in diameter, Nanoshel) with RE. The default weight content of  $\text{Li}_3\text{N}$  for  $\text{Li}_3\text{N}$  SE was 7 wt %, otherwise indicated. High purity Li foil (750  $\mu\text{m}$  thick, 99.9%, Alfa Aesar), Cu foil (Pred Materials), 11  $\mu\text{m}$  thick polyethylene separator (W-Scope), and  $\sim 4$  mAh  $\text{cm}^{-2}$  NMC811 (Targray) were used to make 2032-type coin cells for Li/Li and Li/Cu, and Li/Li<sub>1</sub>Ni<sub>0.8</sub>Co<sub>0.1</sub>Mn<sub>0.1</sub> configured cells.

**DFT Calculation.** The calculations were performed with the DFT code GPAW.<sup>55–57</sup> The electron exchange-correlation was described by Perdew–Burke–Ernzerhof functional within the generalized gradient approximation.<sup>58</sup> The valence electrons are expressed in plane wave basis sets and the core electrons with projector augmented wave (PAW) method. The energy cutoff of 500 eV was applied to all the calculations. The k-point grid of  $3 \times 3 \times 1$  was used for all  $\text{Li}_3\text{N}$ -slab calculations, and  $5 \times 3 \times 1$  was used for Li slab calculations. The energy and forces per atom were converged to within  $10^{-4}$  eV and  $10^{-3}$  eV/Å, respectively. For the slab calculations, the vacuum of 15 Å thickness is used to reduce periodic artificial interactions. The  $\text{Li}_3\text{N}$ -slab consists of six layers of unit cells (spanning approximately 15 Å) in the z-direction. During geometry optimization, the top 4/5/4/4 layers are allowed to relax for Li (110)/ $\text{Li}_3\text{N}$  (001)|(002)/ $\text{Li}_3\text{N}$  (100)/ $\text{Li}_3\text{N}$  (110) adsorption calculations. The diffusion pathways were calculated via the machine-learning nudged elastic band (ML-NEB) using the CatLearn package,<sup>59</sup> with nine images between the initial and the final configurations.

**XRD.** X-ray diffraction (PANalytical Empyrean with a Cu( $K\alpha$ ) X-ray source) was used to examine the crystal structural of  $\text{Li}_3\text{N}$  nanopowder. The  $\text{Li}_3\text{N}$  nanopowders were placed on a glass slide followed by Kapton taping to seal the nanopowders. Then, the diffraction patterns were collected from  $10^\circ$  to  $70^\circ$  using a step size of 0.01.

**SEM/EDXS.** All the samples were rinsed with pure diethyl carbonate (DEC) and dried inside the Ar glovebox before microscopy. SEM was performed using a Thermo Fisher Scientific Apreo S LoVac Scanning Electron Microscope. Micrographs were taken at a potential of 5 kV and beam current of 50 pA, and the electron signal was collected via the Everhart–Thornley Detector (ETD). Energy dispersive X-ray spectroscopy data was collected with

a Bunker XFlash 6–60 detector at a potential of 10 kV and beam current of 800 pA.

**Cryo-TEM.** Cu TEM grids were utilized as the working electrode for  $\text{Li}^0$  electrodeposition from Li/Cu TEM grid cells. 0.1 mAh  $\text{cm}^{-2}$  amount of Li was electrodeposited galvanostatically at 1 mA  $\text{cm}^{-2}$ . After the electrodeposition of  $\text{Li}^0$ , the coin cells were disassembled in an argon-filled glovebox. Then, the electrodeposited TEM grids were rinsed with 60  $\mu\text{L}$  of DEC and dried before freezing the sample with liquid nitrogen. After, the sample was instantly submerged in liquid nitrogen to rapidly expose the sample to cryogen without the ambient exposure. For cryo-TEM characterization, while immersed in liquid nitrogen, the sample was loaded into the Gatan side-entry cryotransfer holder (Gatan model 626) and inserted into the TEM column. The cryo-TEM holder uses a specialized cryoshutter to prevent air exposure and ice condensation onto the sample. Once inside the TEM column, the temperature was maintained at approximately  $-178^\circ\text{C}$ . Cryo-TEM experiments were performed on a Thermo Fisher Titan 80–300 environmental scanning transmission electron microscope operated at an accelerating voltage of 300 kV. The instrument was equipped with an aberration corrector in the image-forming lens, which was tuned before each sample analysis. Cryo-TEM images were acquired by a Gatan K3 IS direct-detection camera in the electron-counting mode. The images were taken with an electron dose rate of around 100  $\text{e}^-/\text{\AA}^2/\text{s}$ , a total of 5 frames were taken with 0.1 s per frame for each image.

**$\text{Li}^+$  Solvation Energy Measurements.** The  $\text{Li}^+$  solvation energies of RE and  $\text{Li}_3\text{N}$  SE were probed by Biologic VMP3 using H-cell that contains control electrolyte (1 M LiFSI in DEC)|salt bridge (1 M LiFSI in DME/DOL)|testing electrolytes (RE and 20 wt %  $\text{Li}_3\text{N}$  SE) with submerged Li metal into the control electrolyte and testing electrolytes. The cell potentials and solvation energies for each of the testing electrolytes were recorded for 3 s to obtain averaged values. The detailed apparatus setup can be found in the literature.<sup>11</sup>

**$^7\text{Li}$  NMR.** An NMR tube with a coaxial insert was used for 1D  $^7\text{Li}$  NMR experiments. The outer tube contained freshly prepared RE and (1–10 wt %)  $\text{Li}_3\text{N}$  SE. The inner tube contained deuterated solutions as external references.  $^7\text{Li}$  NMR was performed on a Varian Inova 500 MHz NMR spectrometer, and the chemical shifts were referenced to 1 M LiCl in D<sub>2</sub>O at 0 ppm.

**Raman.** Raman spectra were collected with a 532 nm green laser at a Horiba XploRA+ confocal microscope. The electrolytes, RE and  $\text{Li}_3\text{N}$  SE, were sealed in quartz cuvettes under Argon environment.

**XPS.** The XPS scans were performed on a PHI Versaprobe I with a monochromatized Al  $K\alpha$  X-ray source. The XPS chamber was kept at a pressure of about  $10^{-7}$  Pa during the measurements. For the sample preparation, electrodeposited  $\text{Li}^0$  on Cu with the capacity and current density of 1 mAh  $\text{cm}^{-2}$  and 1 mA  $\text{cm}^{-2}$  was rinsed with 60  $\mu\text{L}$  of DEC in an Ar filled glovebox. A vacuum transfer vessel was used to transfer the samples directly from the Ar glovebox to the vacuum transfer chamber of the instrument to prevent air exposure. High-resolution spectra were calibrated using the C 1s peak at 284.6 eV.

**Electrochemical Measurements.** The RE (1 M  $\text{LiPF}_6$  in EC:DEC (1:1 v/v) with 10 vol % FEC) and  $\text{Li}_3\text{N}$  SE (1–20 wt %  $\text{Li}_3\text{N}$  in RE) were used for the electrochemical measurements. Twenty  $\mu\text{L}$  of specified electrolytes were used for Li/Li, Li/Li, Li/Li<sub>1</sub>Ni<sub>0.8</sub>Co<sub>0.1</sub>Mn<sub>0.1</sub> cells. The cyclic voltammetry with ultramicroelectrodes for measuring the exchange current density of RE and 20 wt %  $\text{Li}_3\text{N}$  SE was measured by following the literature.<sup>42</sup> In brief, three electrodes were used: Li metal as the reference/counter electrodes and Cu ultramicroelectrode as the working electrode. The scan rate was 20  $\text{V s}^{-1}$ . The voltage window was  $-1.75$  to 2.75 V vs Li/Li<sup>+</sup>. Three measurements were performed to measure averaged exchange current density with statistics. The exchange current density of RE and  $\text{Li}_3\text{N}$  SE was calculated by analyzing the kinetically controlled region in the cyclic voltammograms.<sup>42</sup> The interfacial impedances were measured by Biologics VMP3 with the frequency ranging from 100 mHz to 7 MHz. For the  $\text{Li}^+$  transport number measurements, Li/Li symmetric cells were precycled at 0.5 mA  $\text{cm}^{-2}$  current density and 1 mAh  $\text{cm}^{-2}$  areal capacity for 5 cycles. A constant voltage bias of 10 mV was applied for 1 h to obtain initial ( $I_0$ ) and static ( $I_s$ ) currents.

The interfacial impedance measurements were carried out before and after the constant voltage step to obtain interfacial resistance before ( $R_0$ ) and after ( $R_s$ ). The ionic conductivity of electrolytes was measured by Biologics VMP3 with the frequency ranging from 1 MHz to 100 MHz using symmetric stainless-steel (SS) cells with the 11  $\mu\text{m}$  thick separator (SS/SS cells). The area of 2  $\text{cm}^2$ , distance of 11  $\mu\text{m}$ , and measured solution resistance were used to calculate the ionic conductivity of specified electrolytes. For cycling Li/Cu, Li/Li, and Li/Li<sub>1</sub>Ni<sub>0.8</sub>Co<sub>0.1</sub>Mn<sub>0.1</sub> cells, the measurements were recorded by Arbin and Land instruments. For CE and nucleation overpotential measurements with Li/Cu cells, current density of 0.5  $\text{mA cm}^{-2}$  was applied with cutoff voltage of 1 V. For cyclic voltammetry, Li/Li<sub>1</sub>Ni<sub>0.8</sub>Co<sub>0.1</sub>Mn<sub>0.1</sub> full cells were cycled at 0.1  $\text{mV s}^{-1}$  with the voltage window of 3.0 to 4.5 V vs Li/Li<sup>+</sup> with Biologics VMP3. For the linear sweep voltammetry, the current profiles were obtained from Li/Al cells with RE and Li<sub>3</sub>N SE, in which the used voltage window and sweep rate were 3.0–5.0 V vs Li/Li<sup>+</sup> and 1  $\text{mV s}^{-1}$ . For cycling Li/Li<sub>1</sub>Ni<sub>0.8</sub>Co<sub>0.1</sub>Mn<sub>0.1</sub> full cells, specified charging and discharge C rates were applied with the voltage window of 3.0–4.3 V, where the constant current goes up to 4.2 V and the constant voltage was held at 4.3 V with the cutoff current value of 0.05 C.

## ASSOCIATED CONTENT

### Supporting Information

The Supporting Information is available free of charge at <https://pubs.acs.org/doi/10.1021/acsnano.2c12470>.

Morphologies of electrodeposited Li<sup>0</sup>, XRD measurements of Li<sub>3</sub>N suspension, surface energies of Li<sub>3</sub>N (001) and Li<sup>0</sup> (110) surfaces, <sup>7</sup>Li NMR spectra of RE and Li<sub>3</sub>N SE without LiPF<sub>6</sub>, pictures of 7, 10, and 20 wt % Li<sub>3</sub>N SE, overlaid inverse FFT cryo-TEM image of Figure 4d inset, calculated P/C, F/C, and O/C ratios from XPS for electrodeposited Li<sup>0</sup> with RE and Li<sub>3</sub>N SE, Nyquist plots of Li/Li and Li/Cu cells, ionic conductivities of RE and Li<sub>3</sub>N SE, cyclic voltammograms of Li/Li<sub>1</sub>Ni<sub>0.8</sub>Co<sub>0.1</sub>Mn<sub>0.1</sub> cells with RE and Li<sub>3</sub>N SE, linear sweep voltammetry of RE and Li<sub>3</sub>N SE, averaged values of the interfacial impedances for Li/Li and Li/Cu cells, and averaged Li<sup>+</sup> transport numbers (PDF)

## AUTHOR INFORMATION

### Corresponding Author

**Yi Cui** – Department of Materials Science and Engineering and Department of Energy Science and Engineering, Stanford University, Stanford, California 94305, United States; Stanford Institute for Materials and Energy Sciences, SLAC National Accelerator Laboratory, Menlo Park, California 94025, United States; [orcid.org/0000-0002-6103-6352](https://orcid.org/0000-0002-6103-6352); Email: [yicui@stanford.edu](mailto:yicui@stanford.edu)

### Authors

**Mun Sek Kim** – Department of Materials Science and Engineering and Department of Chemical Engineering, Stanford University, Stanford, California 94305, United States

**Zewen Zhang** – Department of Materials Science and Engineering, Stanford University, Stanford, California 94305, United States; [orcid.org/0000-0002-4909-4330](https://orcid.org/0000-0002-4909-4330)

**Jingyang Wang** – Department of Materials Science and Engineering, Stanford University, Stanford, California 94305, United States; Materials Sciences Division, Lawrence Berkeley Laboratory, Berkeley, California 94720, United States

**Solomon T. Oyakhire** – Department of Chemical Engineering, Stanford University, Stanford, California 94305, United States; [orcid.org/0000-0002-3189-5949](https://orcid.org/0000-0002-3189-5949)

**Sang Cheol Kim** – Department of Materials Science and Engineering, Stanford University, Stanford, California 94305, United States; [orcid.org/0000-0002-1749-8277](https://orcid.org/0000-0002-1749-8277)

**Zhiao Yu** – Department of Chemical Engineering and Department of Chemistry, Stanford University, Stanford, California 94305, United States; [orcid.org/0000-0001-8746-1640](https://orcid.org/0000-0001-8746-1640)

**Yuelang Chen** – Department of Chemical Engineering and Department of Chemistry, Stanford University, Stanford, California 94305, United States; [orcid.org/0000-0002-5249-0596](https://orcid.org/0000-0002-5249-0596)

**David T. Boyle** – Department of Materials Science and Engineering and Department of Chemistry, Stanford University, Stanford, California 94305, United States; [orcid.org/0000-0002-0452-275X](https://orcid.org/0000-0002-0452-275X)

**Yusheng Ye** – Department of Materials Science and Engineering, Stanford University, Stanford, California 94305, United States; [orcid.org/0000-0001-9832-2478](https://orcid.org/0000-0001-9832-2478)

**Zhuojun Huang** – Department of Materials Science and Engineering and Department of Chemical Engineering, Stanford University, Stanford, California 94305, United States; [orcid.org/0000-0001-6236-8693](https://orcid.org/0000-0001-6236-8693)

**Wenbo Zhang** – Department of Materials Science and Engineering, Stanford University, Stanford, California 94305, United States

**Rong Xu** – Department of Materials Science and Engineering, Stanford University, Stanford, California 94305, United States; [orcid.org/0000-0002-3694-595X](https://orcid.org/0000-0002-3694-595X)

**Philaphon Sayavong** – Department of Materials Science and Engineering and Department of Chemistry, Stanford University, Stanford, California 94305, United States

**Stacey F. Bent** – Department of Chemical Engineering, Stanford University, Stanford, California 94305, United States; [orcid.org/0000-0002-1084-5336](https://orcid.org/0000-0002-1084-5336)

**Jian Qin** – Department of Chemical Engineering, Stanford University, Stanford, California 94305, United States; [orcid.org/0000-0001-6271-068X](https://orcid.org/0000-0001-6271-068X)

**Zhenan Bao** – Department of Chemical Engineering, Stanford University, Stanford, California 94305, United States; [orcid.org/0000-0002-0972-1715](https://orcid.org/0000-0002-0972-1715)

Complete contact information is available at: <https://pubs.acs.org/doi/10.1021/acsnano.2c12470>

### Author Contributions

M.S.K. and Y. Cui conceived the idea and conceptualized the work. M.S.K. performed the experiments and analyzed the data with the guidance from Y. Cui. M.S.K. and Y. Cui wrote the manuscript. Z.Z. performed cryo-TEM analysis. J.W. performed DFT calculations. S.T.O. performed XPS analysis. Z.Y. measured the transport number of the electrolytes. Y. Chen performed <sup>7</sup>Li NMR of the electrolytes. S.C.K. measured the solvation energy of the electrolytes. D.B. performed transient voltammetry measurements with ultramicroelectrodes. Y.Y. helped electrochemical measurements. Z.H. performed Raman characterization. W.Z. took SEM images. R.X. performed XRD measurements. P.S. provided helpful discussions. S.F.B. reviewed the manuscript. Y. Cui, Z.B., and J.Q. supervised the overall studies. All the authors discussed the manuscript and provided comments.

### Notes

The authors declare no competing financial interest.

## ACKNOWLEDGMENTS

We acknowledge support from the Assistant Secretary for Energy Efficiency and Renewable Energy, Office of Vehicle Technologies of the US Department of Energy under the Battery Materials Research (BMR) Program and Battery 500 Consortium. Z.Z. acknowledges the support from Stanford Interdisciplinary Graduate Fellowship. S.T.O. acknowledges support from the Knight Hennessy scholarship for graduate studies at Stanford University. J.W. acknowledges computational resources from the Sherlock cluster at Stanford University.

## REFERENCES

- (1) Xiao, J.; Li, Q.; Bi, Y.; Cai, M.; Dunn, B.; Glossmann, T.; Liu, J.; Osaka, T.; Sugiura, R.; Wu, B.; Yang, J.; Zhang, J. G.; Whittingham, M. S. Understanding and Applying Coulombic Efficiency in Lithium Metal Batteries. *Nat. Energy*. **2020**, *5*, 561–568.
- (2) Liu, J.; Bao, Z.; Cui, Y.; Dufek, E. J.; Goodenough, J. B.; Khalifah, P.; Li, Q.; Liaw, B. Y.; Liu, P.; Manthiram, A.; Meng, Y. S.; Subramanian, V. R.; Toney, M. F.; Viswanathan, V. v.; Whittingham, M. S.; Xiao, J.; Xu, W.; Yang, J.; Yang, X. Q.; Zhang, J. G. Pathways for Practical High-Energy Long-Cycling Lithium Metal Batteries. *Nat. Energy*. **2019**, *4*, 180–186.
- (3) Wu, H.; Jia, H.; Wang, C.; Zhang, J. G.; Xu, W. Recent Progress in Understanding Solid Electrolyte Interphase on Lithium Metal Anodes. *Adv. Energy Mater.* **2021**, *11*, 2003092.
- (4) Zheng, J.; Kim, M. S.; Tu, Z.; Choudhury, S.; Tang, T.; Archer, L. A. Regulating Electrodeposition Morphology of Lithium: Towards Commercially Relevant Secondary Li Metal Batteries. *Chem. Soc. Rev.* **2020**, *49*, 2701–2750.
- (5) Lin, D.; Liu, Y.; Cui, Y. Reviving the Lithium Metal Anode for High-Energy Batteries. *Nat. Nanotechnol.* **2017**, *12*, 194–206.
- (6) Kim, M. S.; Zhang, Z.; Rudnicki, P. E.; Yu, Z.; Wang, J.; Wang, H.; Oyakhire, S. T.; Chen, Y.; Kim, S. C.; Zhang, W.; Boyle, D. T.; Kong, X.; Xu, R.; Huang, Z.; Huang, W.; Bent, S. F.; Wang, L. W.; Qin, J.; Bao, Z.; Cui, Y. Suspension Electrolyte with Modified Li<sup>+</sup> Solvation Environment for Lithium Metal Batteries. *Nat. Mater.* **2022**, *21*, 445–454.
- (7) Zachman, M. J.; Tu, Z.; Choudhury, S.; Archer, L. A.; Kourkoutis, L. F. Cryo-STEM Mapping of Solid–Liquid Interfaces and Dendrites in Lithium–Metal Batteries. *Nature*. **2018**, *560*, 345–349.
- (8) Li, Y.; Huang, W.; Li, Y.; Pei, A.; Boyle, D. T.; Cui, Y. Correlating Structure and Function of Battery Interphases at Atomic Resolution Using Cryoelectron Microscopy. *Joule*. **2018**, *2*, 2167–2177.
- (9) Li, Y.; Li, Y.; Pei, A.; Yan, K.; Sun, Y.; Wu, C. L.; Joubert, L. M.; Chin, R.; Koh, A. L.; Yu, Y.; Perrino, J.; Butz, B.; Chu, S.; Cui, Y. Atomic Structure of Sensitive Battery Materials and Interfaces Revealed by Cryo–Electron Microscopy. *Science*. **2017**, *358*, 506–510.
- (10) Wang, H.; Yu, Z.; Kong, X.; Kim, S. C.; Boyle, D. T.; Qin, J.; Bao, Z.; Cui, Y. Liquid Electrolyte: The Nexus of Practical Lithium Metal Batteries. *Joule*. **2022**, *6*, 588–616.
- (11) Kim, S. C.; Kong, X.; Vilá, R. A.; Huang, W.; Chen, Y.; Boyle, D. T.; Yu, Z.; Wang, H.; Bao, Z.; Qin, J.; Cui, Y. Potentiometric Measurement to Probe Solvation Energy and Its Correlation to Lithium Battery Cyclability. *J. Am. Chem. Soc.* **2021**, *143*, 10301–10308.
- (12) Yu, Z.; Wang, H.; Kong, X.; Huang, W.; Tsao, Y.; Mackanic, D. G.; Wang, K.; Wang, X.; Huang, W.; Choudhury, S.; Zheng, Y.; Amanchukwu, C. v.; Hung, S. T.; Ma, Y.; Lomeli, E. G.; Qin, J.; Cui, Y.; Bao, Z. Molecular Design for Electrolyte Solvents Enabling Energy-Dense and Long-Cycling Lithium Metal Batteries. *Nat. Energy*. **2020**, *5*, 526–533.
- (13) Yu, Z.; Rudnicki, P. E.; Zhang, Z.; Huang, Z.; Celik, H.; Oyakhire, S. T.; Chen, Y.; Kong, X.; Kim, S. C.; Xiao, X.; Wang, H.; Zheng, Y.; Kamat, G. A.; Kim, M. S.; Bent, S. F.; Qin, J.; Cui, Y.; Bao, Z. Rational Solvent Molecule Tuning for High-Performance Lithium Metal Battery Electrolytes. *Nat. Energy*. **2022**, *7*, 94–106.
- (14) Hobold, G. M.; Lopez, J.; Guo, R.; Minafra, N.; Banerjee, A.; Shirley Meng, Y.; Shao-Horn, Y.; Gallant, B. M. Moving beyond 99.9% Coulombic Efficiency for Lithium Anodes in Liquid Electrolytes. *Nat. Energy*. **2021**, *6*, 951–960.
- (15) Zhang, Z.; Li, Y.; Xu, R.; Zhou, W.; Li, Y.; Oyakhire, S. T.; Wu, Y.; Xu, J.; Wang, H.; Yu, Z.; Boyle, D. T.; Huang, W.; Ye, Y.; Chen, H.; Wan, J.; Bao, Z.; Chiu, W.; Cui, Y. Capturing the Swelling of Solid-Electrolyte Interphase in Lithium Metal Batteries. *Science*. **2022**, *375*, 66–70.
- (16) Boyle, D. T.; Huang, W.; Wang, H.; Li, Y.; Chen, H.; Yu, Z.; Zhang, W.; Bao, Z.; Cui, Y. Corrosion of Lithium Metal Anodes during Calendar Ageing and Its Microscopic Origins. *Nat. Energy*. **2021**, *6*, 487–494.
- (17) Zhu, Y.; He, X.; Mo, Y. Strategies Based on Nitride Materials Chemistry to Stabilize Li Metal Anode. *Adv. Sci.* **2017**, *4*, 1600517.
- (18) Zhu, Y.; He, X.; Mo, Y. Origin of Outstanding Stability in the Lithium Solid Electrolyte Materials: Insights from Thermodynamic Analyses Based on First-Principles Calculations. *ACS Appl. Mater. Interfaces*. **2015**, *7*, 23685–23693.
- (19) Alpen, U. V. Li<sub>3</sub>N: A Promising Li Ionic Conductor. *J. Solid State Chem.* **1979**, *29*, 379–392.
- (20) Eshetu, G. G.; Judez, X.; Li, C.; Bondarchuk, O.; Rodriguez-Martinez, L. M.; Zhang, H.; Armand, M. Lithium Azide as an Electrolyte Additive for All-Solid-State Lithium-Sulfur Batteries. *Angew. Chem., Int. Ed.* **2017**, *56*, 15368–15372.
- (21) Ren, Y.; Yang, S.; Ma, X.; Qi, Z.; Zhang, C.; Liu, X.; Tan, X.; Sun, S. The Li Ion Transport Behavior in the Defect Graphene Composite Li<sub>3</sub>N SEI: A First-Principle Calculation. *Mater. Today Chem.* **2021**, *21*, 100510.
- (22) Wang, S.; Chen, J.; Lu, H.; Zhang, Y.; Yang, J.; Nuli, Y.; Wang, J. Artificial Alloy/Li<sub>3</sub>N Double-Layer Enabling Stable High-Capacity Lithium Metal Anodes. *ACS Appl. Energy Mater.* **2021**, *4*, 13132–13139.
- (23) Li, Y.; Sun, Y.; Pei, A.; Chen, K.; Vailionis, A.; Li, Y.; Zheng, G.; Sun, J.; Cui, Y. Robust Pinhole-Free Li<sub>3</sub>N Solid Electrolyte Grown from Molten Lithium. *ACS Cent. Sci.* **2018**, *4*, 97–104.
- (24) Chen, K.; Pathak, R.; Gurung, A.; Adhamash, E. A.; Bahrami, B.; He, Q.; Qiao, H.; Smirnova, A. L.; Wu, J. J.; Qiao, Q.; Zhou, Y. Flower-Shaped Lithium Nitride as a Protective Layer via Facile Plasma Activation for Stable Lithium Metal Anodes. *Energy Storage Mater.* **2019**, *18*, 389–396.
- (25) Ghosh, A.; Cherepanov, P.; Nguyen, C.; Ghosh, A.; Kumar, A.; Ahuja, A.; Kar, M.; MacFarlane, D. R.; Mitra, S. Simple Route to Lithium Dendrite Prevention for Long Cycle-Life Lithium Metal Batteries. *Appl. Mater. Today*. **2021**, *23*, 101062.
- (26) Piao, N.; Liu, S.; Zhang, B.; Ji, X.; Fan, X.; Wang, L.; Wang, P. F.; Jin, T.; Liou, S. C.; Yang, H.; Jiang, J.; Xu, K.; Schroeder, M. A.; He, X.; Wang, C. Lithium Metal Batteries Enabled by Synergistic Additives in Commercial Carbonate Electrolytes. *ACS Energy Lett.* **2021**, *6*, 1839–1848.
- (27) Yuan, S.; Bao, J. L.; Wang, N.; Zhang, X.; Wang, Y.; Truhlar, D. G.; Xia, Y. Salt-Rich Solid Electrolyte Interphase for Safer High-Energy-Density Li Metal Batteries with Limited Li Excess. *Chem. Commun.* **2020**, *56*, 8257–8260.
- (28) Yamada, Y.; Wang, J.; Ko, S.; Watanabe, E.; Yamada, A. Advances and Issues in Developing Salt-Concentrated Battery Electrolytes. *Nat. Energy*. **2019**, *4*, 269–280.
- (29) Ren, X.; Zou, L.; Cao, X.; Engelhard, M. H.; Liu, W.; Burton, S. D.; Lee, H.; Niu, C.; Matthews, B. E.; Zhu, Z.; Wang, C.; Arey, B. W.; Xiao, J.; Liu, J.; Zhang, J. G.; Xu, W. Enabling High-Voltage Lithium-Metal Batteries under Practical Conditions. *Joule*. **2019**, *3*, 1662–1676.
- (30) Ren, X.; Chen, S.; Lee, H.; Mei, D.; Engelhard, M. H.; Burton, S. D.; Zhao, W.; Zheng, J.; Li, Q.; Ding, M. S.; Schroeder, M.; Alvarado, J.; Xu, K.; Meng, Y. S.; Liu, J.; Zhang, J. G.; Xu, W.

Localized High-Concentration Sulfone Electrolytes for High-Efficiency Lithium-Metal Batteries. *Chem.* **2018**, *4*, 1877–1892.

(31) Fu, L.; Wang, X.; Chen, Z.; Li, Y.; Mao, E.; Seh, Z. W.; Sun, Y. Insights on “Nitrate Salt” in Lithium Anode for Stabilized Solid Electrolyte Interphase. *Carbon Energy* **2022**, *4*, 12–20.

(32) Wen, Y.; Ding, J.; Yang, Y.; Lan, X.; Liu, J.; Hu, R.; Zhu, M. Introducing  $\text{NO}_3^-$  into Carbonate-Based Electrolytes via Covalent Organic Framework to Incubate Stable Interface for Li-Metal Batteries. *Adv. Funct. Mater.* **2022**, *32*, 2109377.

(33) Gu, S.; Zhang, S. W.; Han, J.; Deng, Y.; Luo, C.; Zhou, G.; He, Y.; Wei, G.; Kang, F.; Lv, W.; Yang, Q. H. Nitrate Additives Coordinated with Crown Ether Stabilize Lithium Metal Anodes in Carbonate Electrolyte. *Adv. Funct. Mater.* **2021**, *31*, 2102128.

(34) Ju, Z.; Yuan, H.; Sheng, O.; Liu, T.; Nai, J.; Wang, Y.; Liu, Y.; Tao, X. Cryo-Electron Microscopy for Unveiling the Sensitive Battery Materials. *Small Sci.* **2021**, *1*, 2100055.

(35) Li, Q.; Xue, W.; Peng, J.; Yang, L.; Pan, H.; Yu, X.; Li, H. Synergistic Effect of Temperature and Electrolyte Concentration on Solid-State Interphase for High-Performance Lithium Metal Batteries. *Adv. Energy Sustainability Res.* **2021**, *2*, 2100010.

(36) Liu, D.; Xiong, X.; Liang, Q.; Wu, X.; Fu, H. An Inorganic-Rich SEI Induced by  $\text{LiNO}_3$  Additive for a Stable Lithium Metal Anode in Carbonate Electrolyte. *Chem. Commun.* **2021**, *57*, 9232.

(37) Zhang, S.; Yang, G.; Liu, Z.; Li, X.; Wang, X.; Chen, R.; Wu, F.; Wang, Z.; Chen, L. Competitive Solvation Enhanced Stability of Lithium Metal Anode in Dual-Salt Electrolyte. *Nano Lett.* **2021**, *21*, 3310–3317.

(38) Lee, D.; Sun, S.; Kim, C.; Kim, J.; Park, K.; Kwon, J.; Song, D.; Lee, K.; Song, T.; Paik, U. Highly Reversible Cycling with Dendrite-Free Lithium Deposition Enabled by Robust SEI Layer with Low Charge Transfer Activation Energy. *Appl. Surf. Sci.* **2022**, *572*, 151439.

(39) Liu, S.; Ji, X.; Piao, N.; Chen, J.; Eidson, N.; Xu, J.; Wang, P.; Chen, L.; Zhang, J.; Deng, T.; Hou, S.; Jin, T.; Wan, H.; Li, J.; Tu, J.; Wang, C. An Inorganic-Rich Solid Electrolyte Interphase for Advanced Lithium-Metal Batteries in Carbonate Electrolytes. *Angew. Chem., Int. Ed.* **2021**, *60*, 3661–3671.

(40) Adams, B. D.; Zheng, J.; Ren, X.; Xu, W.; Zhang, J. G. Accurate Determination of Coulombic Efficiency for Lithium Metal Anodes and Lithium Metal Batteries. *Adv. Energy Mater.* **2018**, *8*, 1702097.

(41) Pei, A.; Zheng, G.; Shi, F.; Li, Y.; Cui, Y. Nanoscale Nucleation and Growth of Electrodeposited Lithium Metal. *Nano Lett.* **2017**, *17*, 1132–1139.

(42) Boyle, D. T.; Kong, X.; Pei, A.; Rudnicki, P. E.; Shi, F.; Huang, W.; Bao, Z.; Qin, J.; Cui, Y. Transient Voltammetry with Ultramicroelectrodes Reveals the Electron Transfer Kinetics of Lithium Metal Anodes. *ACS Energy Lett.* **2020**, *5*, 701–709.

(43) Kim, M. S.; Deepika; Lee, S. H.; Kim, M.-S.; Ryu, J.-H.; Lee, K.-R.; Archer, L. A.; Cho, W. I. Enabling Reversible Redox Reactions in Electrochemical Cells Using Protected  $\text{LiAl}$  Intermetallics as Lithium Metal Anodes. *Sci. Adv.* **2019**, *5*, eaax5587.

(44) Cheng, X. B.; Zhao, M. Q.; Chen, C.; Pentecost, A.; Maleski, K.; Mathis, T.; Zhang, X. Q.; Zhang, Q.; Jiang, J.; Gogotsi, Y. Nanodiamonds Suppress the Growth of Lithium Dendrites. *Nat. Commun.* **2017**, *8*, 336.

(45) Lu, Y.; Tu, Z.; Archer, L. A. Stable Lithium Electrodeposition in Liquid and Nanoporous Solid Electrolytes. *Nat. Mater.* **2014**, *13*, 961–969.

(46) Wang, D.; Zhang, W.; Zheng, W.; Cui, X.; Rojo, T.; Zhang, Q. Towards High-Safe Lithium Metal Anodes: Suppressing Lithium Dendrites via Tuning Surface Energy. *Adv. Sci.* **2017**, *4*, 1600168.

(47) Kamphaus, E. P.; Angarita-Gomez, S.; Qin, X.; Shao, M.; Engelhard, M.; Mueller, K. T.; Murugesan, V.; Balbuena, P. B. Role of Inorganic Surface Layer on Solid Electrolyte Interphase Evolution at Li-Metal Anodes. *ACS Appl. Mater. Interfaces.* **2019**, *11*, 31467–31476.

(48) Bouteau, G.; Van-Nhien, A. N.; Sliwa, M.; Sergeant, N.; Lepretre, J. C.; Gachot, G.; Sagaidak, I.; Sauvage, F. Effect of Standard Light Illumination on Electrolyte’s Stability of Lithium-Ion Batteries Based on Ethylene and Di-Methyl Carbonates. *Sci. Rep.* **2019**, *9*, 135.

(49) Takekawa, T.; Kamiguchi, K.; Imai, H.; Hatano, M. Physicochemical and Electrochemical Properties of the Organic Solvent Electrolyte with Lithium Bis(Fluorosulfonyl)Imide (LiFSI) As Lithium-Ion Conducting Salt for Lithium-Ion Batteries. *ECS Trans.* **2015**, *64*, 11–16.

(50) Soto, F. A.; Ma, Y.; Martinez De La Hoz, J. M.; Seminario, J. M.; Balbuena, P. B. Formation and Growth Mechanisms of Solid-Electrolyte Interphase Layers in Rechargeable Batteries. *Chem. Matter.* **2015**, *27*, 7990–8000.

(51) Henschel, J.; Peschel, C.; Klein, S.; Horsthemke, F.; Winter, M.; Nowak, S. Clarification of Decomposition Pathways in a State-of-the-Art Lithium Ion Battery Electrolyte through  $^{13}\text{C}$ -Labeling of Electrolyte Components. *Angew. Chem., Int. Ed.* **2020**, *59*, 6128–6137.

(52) Hobold, G. M.; Khurram, A.; Gallant, B. M. Operando Gas Monitoring of Solid Electrolyte Interphase Reactions on Lithium. *Chem. Matter.* **2020**, *32*, 2341–2352.

(53) Saurel, D.; Orayech, B.; Xiao, B.; Carriazo, D.; Li, X.; Rojo, T. From Charge Storage Mechanism to Performance: A Roadmap toward High Specific Energy Sodium-Ion Batteries through Carbon Anode Optimization. *Adv. Energy Mater.* **2018**, *8*, 1703268.

(54) Kim, M. S.; Ryu, J. H.; Deepika; Lim, Y. R.; Nah, I. W.; Lee, K. R.; Archer, L. A.; Cho, W. I. Langmuir–Blodgett Artificial Solid-Electrolyte Interphases for Practical Lithium Metal Batteries. *Nat. Energy.* **2018**, *3*, 889–898.

(55) Mortensen, J. J.; Hansen, L. B.; Jacobsen, K. W. Real-Space Grid Implementation of the Projector Augmented Wave Method. *Phys. Rev. B Condens. Matter Mater. Phys.* **2005**, *71*, 035109.

(56) Enkovaara, J.; Rostgaard, C.; Mortensen, J. J.; Chen, J.; Dulak, M.; Ferrighi, L.; Gavnholt, J.; Glinsvad, C.; Haikola, V.; Hansen, H. A.; Kristoffersen, H. H.; Kuisma, M.; Larsen, A. H.; Lehtovaara, L.; Ljungberg, M.; Lopez-Acevedo, O.; Moses, P. G.; Ojanen, J.; Olsen, T.; Petzold, V.; Romero, N. A.; Stausholm-Møller, J.; Strange, M.; Tritsarlis, G. A.; Vanin, M.; Walter, M.; Hammer, B.; Häkkinen, H.; Madsen, G. K. H.; Nieminen, R. M.; Nørskov, J. K.; Puska, M.; Rantala, T. T.; Schiøtz, J.; Thygesen, K. S.; Jacobsen, K. W. Electronic Structure Calculations with GPAW: A Real-Space Implementation of the Projector Augmented-Wave Method. *J. Phys.: Condens. Matter.* **2010**, *22*, 253202.

(57) Hjorth Larsen, A.; Jørgen Mortensen, J.; Blomqvist, J.; Castelli, I. E.; Christensen, R.; Dulak, M.; Friis, J.; Groves, M. N.; Hammer, B.; Hargus, C.; Hermes, E. D.; Jennings, P. C.; Bjerre Jensen, P.; Kermode, J.; Kitchin, J. R.; Leonhard Kolsbjerg, E.; Kubal, J.; Kaasbjerg, K.; Lysgaard, S.; Bergmann Maronsson, J.; Maxson, T.; Olsen, T.; Pastewka, L.; Peterson, A.; Rostgaard, C.; Schiøtz, J.; Schütt, O.; Strange, M.; Thygesen, K. S.; Vegge, T.; Villhelmsen, L.; Walter, M.; Zeng, Z.; Jacobsen, K. W. The Atomic Simulation Environment - A Python Library for Working with Atoms. *J. Phys.: Condens. Matter.* **2017**, *29*, 273002.

(58) Perdew, J. P.; Burke, K.; Ernzerhof, M. Generalized Gradient Approximation Made Simple. *Phys. Rev. Lett.* **1996**, *77*, 3865.

(59) Garrido Torres, J. A.; Hansen, M. H.; Jennings, P. C.; Boes, J. R.; Bligaard, T. Low-Scaling Algorithm for Nudged Elastic Band Calculations Using a Surrogate Machine Learning Model. *Phys. Rev. Lett.* **2019**, *122*, 156001.